# Rockwall permafrost dynamics evidenced by Repeated and Automated Electrical Resistivity Tomography at Aiguille du Midi (3842 m a.s.l., French Alps)

Feras Abdulsamad[1, 2], Josué Bock[1], Florence Magnin[1], Emmanuel Malet[1], André Revil[1], Matan Ben-Asher[1], Jessy Richard[1, 2], Pierre-Allain Duvillard[2], Marios Karaoulis[3], Thomas Condom[4], Ludovic Ravanel[1] and Philip Deline[1]

1. EDYTEM, CNRS - Université Savoie Mont-Blanc, 73370 Le Bourget du Lac, France
2. Naga Geophysics, 229 rue Joseph Fontanet 73000 Chambéry, France
3. School of Geology, Geophysics Department, Aristotle University of Thessaloniki, Thessaloniki, Greece
4. Univ. Grenoble Alpes, IRD, CNRS, INRAE, Grenoble-INP, IGE, 38000 Grenoble, France

**Corresponding author:** Abdulsamad Feras (feras.abdul-samad@univ-smb.fr)

**Emails:** feras.abdul-samad@naga-geophysics.com; andre.revil@univ-smb.fr; ludovic.ravanel@univ-smb.fr; florence.magnin@univ-smb.fr; mkaraoulis@geo.auth.gr; matan.ben-asher@univ-smb.fr; pierre-allain.duvillard@naga-geophysics.com; josue.bock@laposte.net; emmanuel.malet@univ-savoie.fr; jessy.richard@naga-geophysics.com; thomas.condom@ird.fr; philip.deline@univ-smb.fr

**Keywords:** Rockwall permafrost dynamics; Active layer thickness; Electrical resistivity tomography; Temperature measurements.

*Intended for publication in The Cryosphere*

**Abstract.** Permafrost degradation significantly affects the stability of rockwalls in high altitude regions. Monitoring rockwall permafrost is essential for assessing potential geohazards. While borehole temperature measurements are the most direct permafrost monitoring approach, they lack sufficient spatial representation in such highly heterogeneous ground conditions. Conversely, geoelectrical measurements can provide more comprehensive insights into these complex patterns and dynamics. This study investigates the permafrost dynamics and intends to detect potential hydrogeological processes at the Aiguille du Midi (3842 m a.s.l., French Alps) using repeated and Automated-Electrical Resistivity Tomography (A-ERT) approaches, covering a period of 3.5 years (06/2020-12/2023). A total of three geoelectrical profiles have been installed on three faces of the Aiguille du Midi (N-W, S and E). An automated acquisition system for permanent resistivity monitoring and remote data acquisition is implemented. A time-lapse inversion technique is employed to get the temporal and spatial variations of electrical resistivity at seasonal and interannual time scales. The data revealed significant variations in active layer thickness across rock faces, along with a slight decrease in electrical resistivity at depth, indicating permafrost warming over time. However, they did not provide clear evidence of water pressurization in rock fractures. Using a petrophysical model, calibrated with laboratory measurements of the temperature dependence of electrical resistivity of granite sample, we estimated the temperature within the frozen zone from the resistivity measurements, under favorable conditions at surface in summer and autumn. Validation against direct temperature measurements in a 10-m depth borehole along the NW profile indicates a mean absolute error less than 1 °C within the frozen zone. This research underscores the efficacy of ERT as a promising, non-invasive tool for quantitative monitoring of permafrost dynamics in Alpine environments. It also reveals challenges associated with conducting A-ERT in high mountain rockwalls where the contact resistance is very high (~500 kΩ) and sometimes intermittent due to factors such as thunder strikes and rockfalls.

# 1. Introduction

Climate change accelerates the degradation of the permafrost in high-mountains areas worldwide (Smith et al., 2022). In the European Alps, permafrost has warmed up to > 1°C at 10 m depth, especially in bedrock permafrost (Etzelmüller et al., 2020; Magnin et al., 2024; Noetzli et al., 2024). Over the last decade, there has been a continuous increase in rockfall events, particularly those impacting permafrost in the European Alps (Cathala et al., 2024; Jacquemart et al., 2024; Ravanel et al., 2017). Infrastructure located in high altitude are increasingly affected by these events (Duvillard et al., 2021, 2018; Hartmeyer et al. 2020). Permafrost degradation of the rock mass can also locally be accelerated by heat advection through water infiltration in fractures (see for example Hasler et al., (2011) for a laboratory experiment; Magnin and Josnin (2021) for a numerical experiment), leading to erosion of the ice-infill (Hauck and Hilbich, 2024; Hartmeyer et al. 2020). As a result, a loss of bonding between rock and ice may occur, which in turn alters the mechanical properties of such assemblage (Mamot et al., 2018; Krautblatter et al., 2013). Therefore, understanding the thermo-hydrogeological dynamics of steep Alpine rock faces is essential for assessing potential geohazards associated with permafrost degradation.

To assess permafrost warming, one approach is to directly determine and monitor rockwall temperatures using temperature sensors installed at the rock surface or in boreholes (*e.g.*, Magnin et al., 2024). Although borehole temperature monitoring is still the only direct method to detect and monitor permafrost, it provides only point-scale information, while its distribution and evolution can be highly variable in extreme topographical conditions. In addition, boreholes in rockwall at high altitude are logistically difficult to realize. and are also expensive and invasive.

On the other hand, geophysical measurements provide higher spatial coverage with respect to boreholes. Various non- or minimally intrusive methods have been applied to

evaluate permafrost, including Refraction Seismic Tomography (RST) (*e.g.*, Steiner et al., 2019; Draebing 2016), Ground Penetrating Radar (GPR) (Campbell et al., 2018), Electrical Resistivity Tomography (ERT) (*e.g.*, Mollaret et al., 2020; Krautblatter and Hauck 2007) and Induced Polarization (IP) (Maierhofer et al., 2024; Abdulsamad et al., 2019; Duvillard et al., 2018; Doetsch et al., 2015). Combined geophysical methods can take advantage of the complementary petrophysical and spatial sensitivities of these different methods. For instance, ERT measurement was combined with RST to evaluate ice, air, water, and rock contents (Mewes et al., 2017; Hauck et al., 2011). Recently, joint inversion of ERT and RST could reduce the uncertainties in the evaluation of air, water, ice and rock contents (Pavoni et al., 2023; Steiner et al., 2021; Mollaret et al., 2020; Wagner et al., 2019). IP measurements (providing tomograms of the electrical conductivity and normalized chargeability) have been recently used to assess the distribution of permafrost temperature, relying on laboratory calibration and a petrophysical (physics-based) model connecting resistivity and normalized chargeability with temperature under frozen and unfrozen conditions (see Moser et al., 2025; Duvillard et al., 2021, 2018; Revil et al. 2026a, b and references therein).

In the last two decades, ERT has become an increasingly popular tool in permafrost studies (*e.g.*, Herring et al., 2023; Farzamain et al., 2020; Magnin et al., 2015a; Krautblatter et al., 2010). Herring et al. (2023) provide a review of the use of ERT method in permafrost research, detailing both the advantages and limitations of this method in such a context. A significant advantage of using electrical resistivity measurements to assess mountain permafrost is that the freezing and thawing of water filling pores are associated with considerable changes in resistivity (generally between one to three orders of magnitude, see Coperey et al., 2019). Because of this sensitivity, electrical resistivity tomograms can be used to assess the presence and distribution of permafrost.

Repeated ERT measurements at specific time intervals using the same survey geometry can be used to track the temporal and spatial evolution of permafrost over time (*e.g.*, Offer et al., 2025, Hilbich et al., 2008). However, rapid changes due to water flow, infiltration or drainage (such as during snowmelt or rainfall) may not be captured by monthly or seasonally repeated measurements (Krautblatter et al., 2010). Alternatively, continuous resistivity measurements, known as Automated-ERT (A-ERT) or ERT monitoring, offer the ability to track the ongoing evolution of permafrost and capture rapid, heterogeneous and non-linear changes in its temperature and ice content (*e.g.*, Scandroglio et al., 2021; Doetsch et al., 2015). A-ERT over period of several years has been recently used to track the degradation of permafrost associated with global warming (Mollaret et al., 2019; Keusching et al., 2017; Doetsch et al., 2015; Hilbich et al., 2008).

Furthermore, the time-lapse inversion of geophysical data derived from a fixed monitoring network provides a succession of tomograms showing the spatial and temporal changes in subsurface resistivity (see; Karaoulis et al., 2013; Loke, 1999). The results of time-lapse inversions of apparent resistivity data can be directly linked to the evolution of permafrost throughout the annual cycle or to rapid variations caused by water infiltration or drainage during short periods of time (Cimpoiasu et al., 2025; Keusching et al., 2017; Hilbich et al., 2008).

That said, A-ERT at high altitudes (>3500 m) and over a multi-profile setting has not yet been tested for pluriannual permafrost monitoring. The use of A-ERT under high-altitude conditions presents specific challenges due to extreme topographical and climatic conditions as well as meteorological events. However, it could provide valuable information about the hydrogeological system and the evolution of permafrost in environments where its distribution and dynamic are highly heterogeneous.

In this study, we present the results of an A-ERT survey conducted over nearly four years (2020-2023) at Aiguille du Midi (AdM) in the Mont-Blanc massif (French Alps). The site

consists of massive and fractured granite and includes infrastructure such as tunnels and elevators. Water infiltration was observed at various locations within the tunnels. The objective of this study is to investigate permafrost dynamics from infra-seasonal to multiyear timescales and through various rock faces of the same site. Our goals are: (1) evaluating the potential of A-ERT to characterize seasonal to pluriannual permafrost dynamics, their heterogeneity and non-linearity in steep alpine rockwalls; (2) assessing the accuracy of temperature derived from resistivity measurements; and (3) attempting to detect potential water circulation pathways in fractures, along with their thermal impacts. For this objective, a total of three ERT profiles were deployed downwards from the summit in three directions: North-West (NW), South (S) and East (E). Each profile consists of 32 electrodes spaced at 5 m. In addition to field data, laboratory resistivity measurements were conducted on granite core samples, in both unfrozen and frozen conditions. Furthermore, temperature was continuously monitored in a 10 m-deep borehole along the NW profile and was used to quantitatively evaluate the accuracy of temperature estimates derived from geophysical measurements of electrical resistivity.

## 2. Study site

We investigate the Aiguille du Midi (3842 m a.s.l.), which is the highest and most western summit of the Aiguilles de Chamonix (Fig. 1a). It is located on the NW flank of the Mont-Blanc massif. It includes three peaks that are all connected by human-made bridges and galleries and hosts major touristic and technical infrastructures. During the summer season, AdM is visited by approximately 5000 visitors per day, who are transported from the city of Chamonix by cable car, making it one of the most intensively frequented high-alpine sites in the European Alps. Since the 1950s, the morphology and appearance of the summit have been strongly modified by construction and infrastructure development (Fig. 1). These factors, combined with the extreme topography characterized by near-vertical rock walls with an average slope of 78° on the northwestern face, make the site particularly prone to rock

instability processes. Consequently, AdM represents a critical location where geotechnical and geophysical monitoring is essential to ensure the long-term stability of the infrastructures and the safety of visitors. Our study focuses on the central peak, which is the highest among the three, and which hosts the cable-car station connecting AdM to Pointe Helbronner with the *Panoramic Mont-Blanc* cable car.

The lithology in the study area is dominated by massive granite with a very low porosity (~ 0.01, Magnin et al., 2015a). The highest parts (3740 to 3840 m a.s.l.) of the peak tend to be steep, contain few large fractures, and, in places, are characterized by vertical foliation bands and small cracks (Magnin et al., 2015b). Figure 2 shows the mean monthly and annual air temperature at AdM during the study period. The year 2021 was the coolest year (yearly averages: -5.8 °C, -6.9 °C, -5.3 °C, and -5.7 °C from 2020 to 2023, respectively), and 2022 was the warmest especially due to extremely warm summer that had important consequences on rock temperature (Magnin et al., 2024; Bruel et al., 2026).

In order to evaluate the thermal state and the distribution of permafrost at AdM, three boreholes have been drilled in 2009. They are labeled BH-NW on the NW face, BH-S on the South face and BH-E on the East face. Each borehole is 10-m-deep and 66 mm in diameter and was drilled normal to the topography (their position is shown in Fig. 1b-d). Each borehole is equipped with 15-thermistor strings calibrated in an ice-water bath and then placed at different depths in the borehole.

The temperature of the permafrost core shows significant variability between the South and North-West faces of the AdM. For example, at a depth of 10 meters, the temperature is approximately -4 °C on the NW face, while it is around -1 °C on the sun-exposed S face (Magnin et al., 2024). These temperature differences indicate the presence of strong temperature gradients within the rock mass. In the same way, the Active Layer Thickness (ALT, *i.e.*, the maximum seasonal thaw layer) is also highly variable as interpolated between

175 temperature sensors: it is observed to be around 1.3 to 2.7 m in summer on the NW side, while
176 it reaches 4.8 to 7.6 m on the S side in the early fall. Below this depth, permafrost is present
177 (Magnin et al., 2024). Figure A1 (appendix A) shows the temperature variation over depth in
178 boreholes BH-NW and BH-S on different dates.

179 BH-NW is located along an electrical resistivity profile (NW profile) and is positioned
180 between electrodes 8 and 9 (counted from the bottom) of the NW profile (see Fig. 1c). The
181 temperature measured in this borehole is used to assess the accuracy of the temperature derived
182 from ERT results using the petrophysical model presented in the next section.

183

184

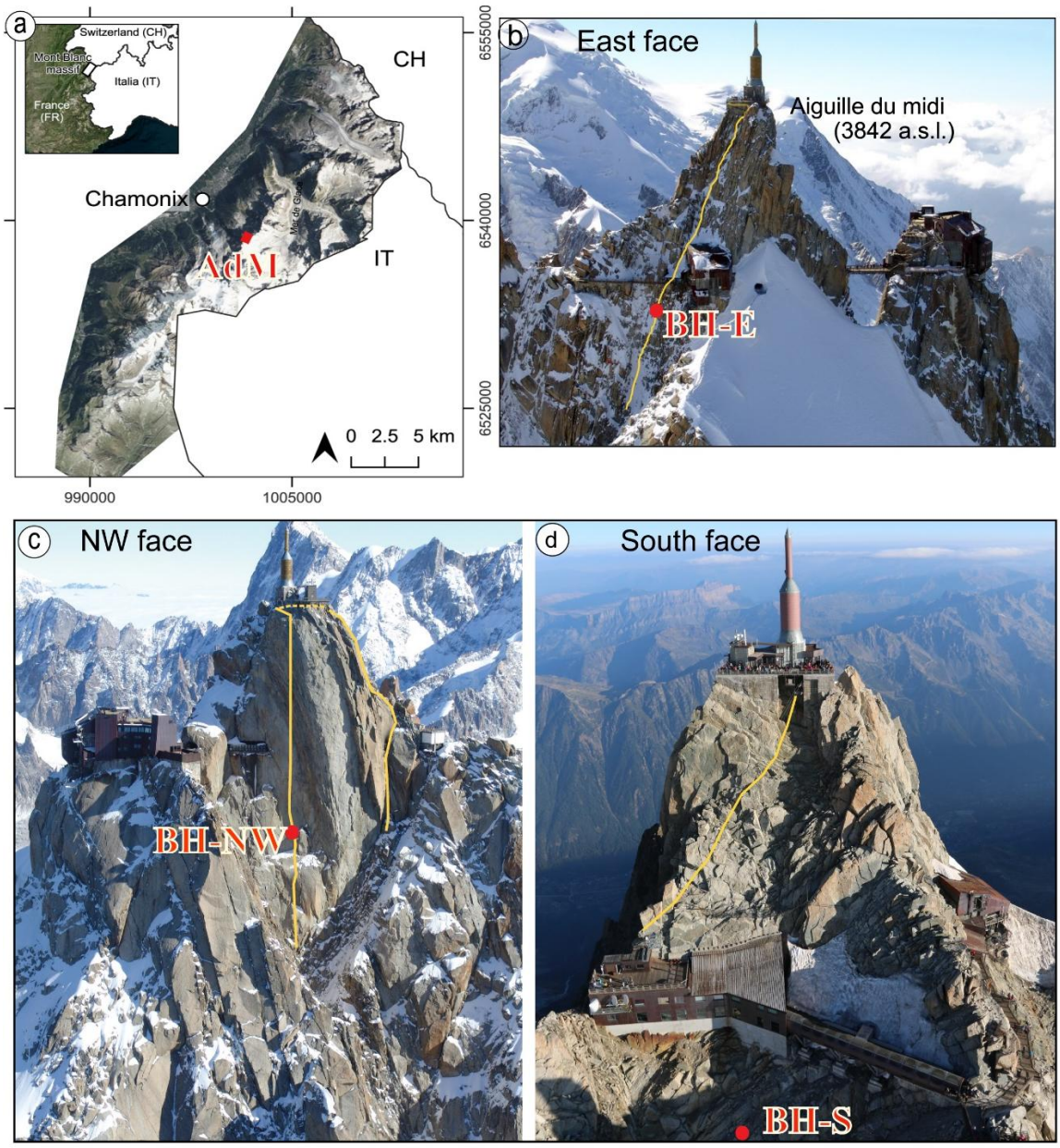


185

186 **Figure 1.** Study site location and geophysical survey setting. The yellow lines indicate the approximate
187 positions of electrical resistivity profiles on each side (NW, E and S profiles). The red dots denote the
188 borehole locations. (a) Location of the study site (Aiguille du Midi (AdM)), in the Mont Blanc massif
189 (here, the French side). The electrical resistivity profile and borehole locations at the East face(b), at the
190 North-West face (c) and at the South face (d).

191

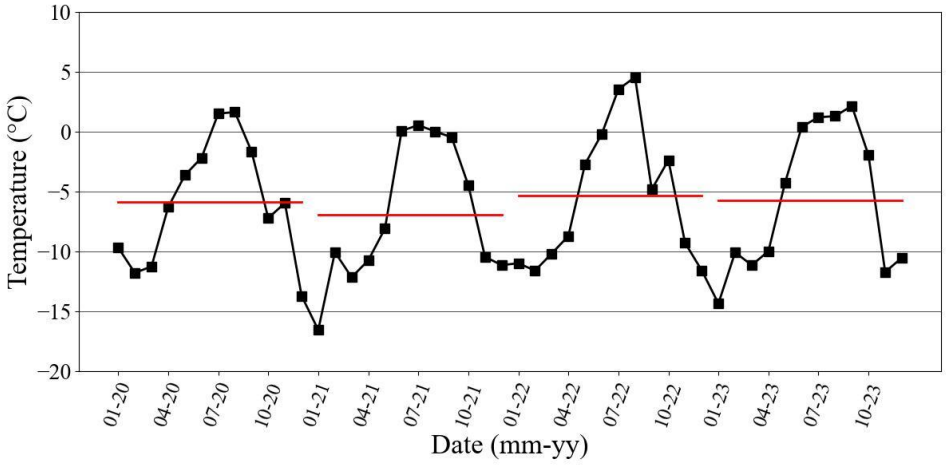


**Figure 2.** Monthly average air temperature (°C) at AdM during the survey period (Data from the meteorological station of Institute of Environmental Geosciences at the Aiguille du Midi). Horizontal bars show the annual average air temperature.

## 3. Electrical conductivity - temperature relationship

The electrical conductivity of a rock represents its ability to conduct an electrical current under the application of an imposed electrical field. The electrical conductivity (inverse of the electrical resistivity) of a rock depends on its porosity $\phi$ (dimensionless), water content $\theta$ (dimensionless), pore water conductivity, Cation Exchange Capacity (CEC), and rock temperature $T$ (in °C) (*e.g.*, Revil et al., 1998).

Above the freezing point (typically, but not necessary, around 0°C), electrical conductivity ($\sigma(T)$ in S m$^{-1}$) increases linearly with temperature according to Revil et al. (1998):

$$\sigma(T) = \sigma(T_0)\left[1 + \alpha_T (T - T_0)\right], \qquad (1)$$

where $\alpha_T$ = 0.021±0.02 °C$^{-1}$, $T_0$ = 25°C denotes the reference temperature, and $\sigma(T_0)$ denotes the conductivity of the rock at the reference temperature. Equation (1) results from the effect of temperature on the mobility of the ions in the pore water and in the electrical double layer coating the surface of the grains.

In contrast, under freezing conditions, temperature variations have a significant influence on electrical conductivity because of the occurrence of an insulating phase (*i.e.*, ice formation) in the pore space and despite the increase in the salinity of the pore water with temperature decrease. This temperature dependence of electrical conductivity can be modeled as follows (see details in Duvillard et al., 2018; 2021; Coperey et al., 2019):

$$\sigma(T) \approx \left[ \left(\phi - \theta_r\right) \exp\left( -\frac{T - T_F}{T_C} \right) + \theta_r \right] \frac{\sigma(T_0)}{\phi} \left[1 + \alpha_T (T - T_0)\right], \qquad (2)$$

where $\theta_r$ (dimensionless) denotes the residual water content when T<<$T_F$, $T_F$ denotes the liquidus or freezing point/temperature, $T_C$ denotes a characteristic temperature controlling the transition between the unfrozen state and the frozen state, and $\phi - \theta_r$ denotes the maximum volumetric ice content at low temperatures. Equation (2) provides the opportunity to convert electrical conductivity or electrical resistivity tomogram measured in the field to a temperature distribution (*e.g.*, Duvillard et al., 2021).

# 4. Methods

## 4.1 Laboratory measurements

In order to calibrate our field measurements and evaluate the parameters (*e.g.,* $T_C$, $\theta_r$) in the petrophysical model discussed above (Section 3), we conducted an electrical conductivity experiment on a granite rock sample collected from an outcrop at the study site. The cube-shaped granite sample (dimensions: 5 × 5 × 5 $cm^3$) was dried during 24 h at approximately 100 °C, then saturated under vacuum with degassed water. The saturated water conductivity was 0.016 S $m^{-1}$ at equilibrium at $T$ = 25°C. This value is representative of the conductivity of infiltrating water collected and measured in galleries at the AdM site (approximately 150 µS/cm or 0.015 S $m^{-1}$, see Ben-Asher et al. (2026). The sample was left in the solution for several

weeks to reach chemical equilibrium before performing the laboratory measurements. The sample was characterized by a very low measured porosity $\phi = 0.014$.

For thermal-resistivity analysis, the sample was placed in a heat-resistant insulating bag immersed in a thermostat bath (KISS K6 from Huber; dimensions: 210×400×546 $mm^3$; bath volume: 4.5 L). The temperature of the bath was controlled with a precision of 0.1 °C. Glycol was used as the heat carrying fluid (Coperey et al., 2019). Thin Carbon film electrodes were used for both current injections and potential measurement. The complex conductivity spectra were obtained over the temperature range of +10 to −10 °C, using a high-precision impedance-meter ZEL-SIP04-V02 (Zimmermann et al., 2008). The resistivity measurements reported here are at a frequency of 1 Hz (Coperey et al., 2019).

### 4.2 ERT Data acquisition

ERT has been conducted over a four-years period (06/2020 - 12/2023). A total of three cables, each with 32 take-outs spaced 5 m (for a profile length of 155 m), were installed. The three cables were deployed downwards from the summit in three directions: North-West (NW), East (E) and South (S). The S profile starts at the South side and passes to the North-West side around mid-distance (see Fig. 1c, d). The cables were installed gradually (over a year) starting from NW side (installed in June 2020), then on the South side (installed in July and August 2020), and finally on the East side (installation finished in March 2021 because of snowpack in 2020 at this side). In order to ensure good electrical contact between electrodes and rock mass, stainless steel (A4/316) climbing bolts (Fischer 10×126 mm) poured in salty bentonite were used and placed firmly in holes drilled in the rock. A specially designed jumper was used to attach each take-out to the bolt to ensure maximum contact. The resistivity cables were attached to anchors to minimize damage from rockfall and snow pressure.

A LS2-Terrameter (ABEM) with internal impedance of 20 MΩ was used for the data acquisition. The ERT device and control system for monitoring were deployed inside the summit station with network access, power connection, and overvoltage protection. Data acquisition was fully automated and remotely controlled since September 2021. Finally, the position of every electrode was measured using a differential GPS when the signal is available and a theodolite in steep areas. The measurements were carried out using a Wenner configuration, which provides a high signal-to-noise ratio and is widely used in mountain permafrost environments (Mollaret et al., 2020; Krautblatter and Hauck, 2007; Dahlin and Zhou, 2004). Each profile consists of 155 data points. An injected current ranging from 0.1 mA to 200 mA was applied, with a maximum stack number of 4 was applied to ensure a standard deviation of less than 5 % in the measured resistivity. The first measurements were performed in June 2020. Between June 2020 and September 2021, ERT measurements were repeated occasionally. Then the continuous measurements started in late September 2021 after developing an automated system of acquisition. Datasets were daily recorded for each profile (NW, S and E profiles).

A Contact Resistance (CR) test was performed before each series of measurements. A high contact resistance in the rock wall (>100 kΩ) was encountered throughout the entire survey period, which posed a challenge to the quality and continuity of data acquisition. CR varies between a few kΩ and 10 000 kΩ. However, beyond a CR threshold, the ERT measurements lose their accuracy. Electrodes with high CR (>600 kΩ) are excluded automatically by the LS2, leading to gaps in the pseudo-section of apparent resistivity. Special efforts were made to reduce CR and improve the electrode/rock contact, including the addition of salty water, using copper electrodes and duplicate electrodes. The latter one resulted in a significant and durable improvement in CR (one order of magnitude reduction in CR). Figure B1 shows the temporal evolution of CR at profiles S and NW, as well as gaps in the A-ERT measurements caused by

cable defects. It also indicates the date of duplicate electrode installation, highlighting a reduction in contact resistance following installation.

The A-ERT ran into numerous software and hardware issues, resulting in unsystematic data gaps. The E face cable was severely damaged by a lightning strike, before being destroyed by an uncontrolled rock purge. Additionally, NW and S cables were both damaged by rockfalls, leading to significant data gaps (see Fig. 3 and Fig. B1). Repairing or replacing the damaged cables was not possible for several reasons (e.g., limited access to the cable path because of accumulated snowpack). Data acquisition on the Eastern side (E profile) encountered numerous challenges related to contact resistance, rockfalls and cable connections, resulting in long gaps and insufficient data for long time analysis or time-lapse inversion.

### 4.3. Data processing and inversion

The apparent resistivities were calculated using the open-source package pyGIMLi (Rücker et al., 2017), which combines measured resistances and electrode positions. For datasets used in inversion, a systematic quality-control procedure was applied prior to processing. The primary selection criterion was the number of connected electrodes within each pseudo-section. Up to four unconnected electrodes (typically due to high contact resistance) were tolerated, depending on their positions, since electrode contributions are not equal in the pseudo-section. After selecting valid datasets, outlier removal was performed. To define appropriate filtering threshold, we individually analyzed representative pseudo-sections acquired in autumn and spring (completed datasets). As a result of this analysis, we filtered outliers out of the range (300 Ωm - 20 kΩm) for data measured in summer and autumn, and out of range (300 Ωm - 200 kΩm) for data measured in spring and winter. Table C1 (appendix C) summarizes the data presented in this study. In most cases, more than 80 % of the originally recorded data points were retained in each pseudo-section after filtering.

The inversion of the electrical resistivity datasets was performed using the open-source package pyGIMLi (Rücker et al., 2017; Günther et al., 2006). The inversion uses a Gauss-Newton minimization algorithm of a cost-function penalizing the roughness of the electrical resistivity distribution on an irregular grid (Günther et al., 2006). In the absence of a reciprocal dataset to estimate errors in measurements, we used a linear error model which assumed 5 % relative error and absolute error 1e-5. The parameters used in the inversion process are zWeight = 10 and smoothness (lambda) equal one. The inversion parameter zWeight is chosen higher than one to enhance the vertical discontinuities and vertical structures (*i.e.,* to better delineate the active layer and infrastructures), during the inversion process. Following Mollaret et al. (2020), an iterative process was conducted to select the smoothness parameter (lambda) that minimizes the data misfit of individual inversions of a reference dataset (dataset of 30/06/2020). The root-mean-square (RMS) error is evaluated at the end of each inversion and reported at the figures. In order to track the seasonal and interannual variations in the permafrost, a time-lapse inversion approach was employed. In this case, the reference model was moved along with the inversion so that the difference to the preceding step is constrained (Doetsch et al., 2015; Karaoulis et al., 2013).

# 5. Results and interpretation

Selected datasets are presented below to address the objectives of this study, including the characterization of the general structure, seasonal variations, and the hydrogeological system.

## 5.1. Overview of the raw data

Our interpretation of the ERT data starts with an analysis of the measured apparent resistivity data, which can provide insights into subsurface conditions. Figure 3 shows the temporal distribution of the measured apparent resistivities and the averaged apparent resistivity

along the S-profile, with examples of time series of measured apparent resistivities obtained using various quadrupole configurations (ABMN), shown in different colors. The majority of measured apparent resistivities are distributed over three orders of magnitude (100 Ω.m to 100 kΩ.m), with few data points out of this range.

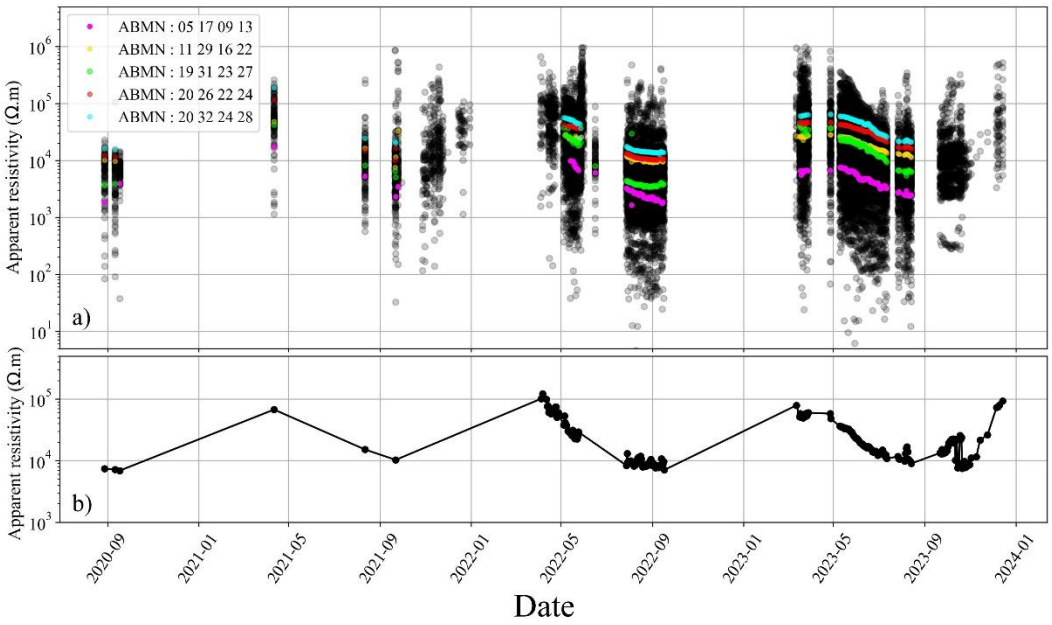


**Figure 3.** Distribution of measured apparent resistivity. a) daily distribution of the apparent resistivity over time at the S face (approximately 300 datasets). Colored lines present examples of resistivity times series, each corresponding to a different set of quadrupoles (AMNB). b) Mean daily measured apparent resistivity at the S face.

Figure 4 shows the variations in the average apparent resistivity associated with the same electrode distance or pseudo-depth for three selected datasets from two profiles (NW and S profiles). The data reveal the interannual and seasonal variations in the measured apparent resistivity, as well as the differences between the two sides. During frozen conditions at the surface (dataset from 12-04-2021), the apparent resistivity is almost the same on both sides (~100 to 120 kΩm near the surface), with only a slight decrease with depth at both sides. At the end of summer (dataset from 17-09-2021 and 25-09-2021), the resistivity values are higher in 2021 than in 2020 on both sides, which correlates with climatic data indicating that 2021 was a

cooler year, on average (see Fig. 2). Secondly, on the NW face, the average resistivities increase with depth (from ~7 kΩ.m to ~12 kΩ.m), while on the south side, the average resistivities decrease with depth (approximately 13 kΩ.m at shallow depth to ~7 kΩ.m at greater depth). This difference in trend between the two sides can be attributed to cooler conditions on the north-face, where permafrost appears at shallow depth, and warmer conditions on the south-face, characterized by a drained and thicker thawed active layer. This observation is consistent with the temperature measurements from boreholes BH-NW and BH-S (see Fig. A1).

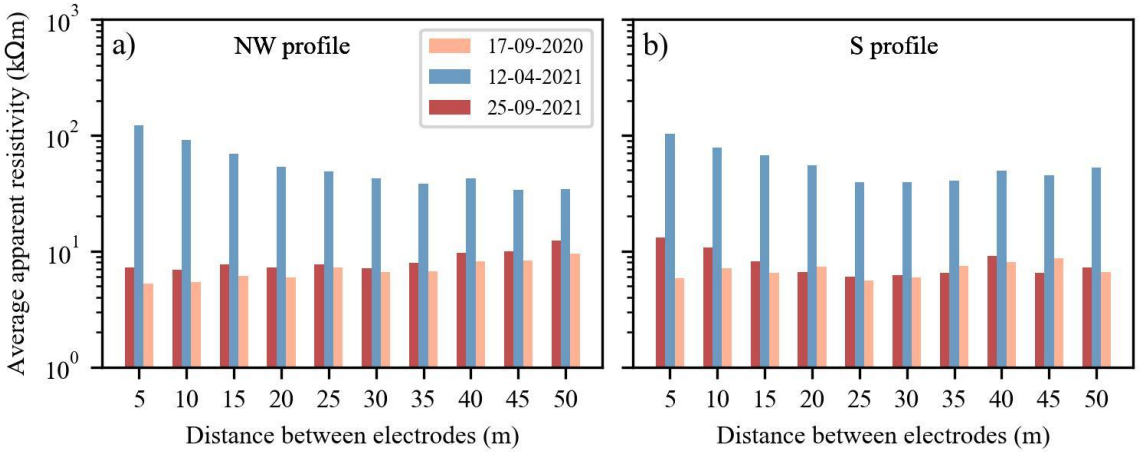


**Figure 4.** Seasonal variations of the average apparent resistivity at different distances between electrodes within a quadrupole (*i.e.*, at varying depths of investigation). Data in spring shows the same pattern on both sides. In autumn, there is a divergence in the trend of average resistivities with depth on both sides, that is related to the hydrothermal conditions at each side.

## 5.2. Internal structure of the site

In order to gain an overview of the internal structure of the study site based on the resistivity distribution, we carried out inversions of the first dataset acquired along two long profiles (NW+S and NW+E), using Wenner electrode arrays with 64 electrodes (Figs. 5 and 6). Figure 5 shows the electrical resistivity tomogram from late summer 2020 (August 26th, 2020), where acquisition on both North-West and South sides (NW+S) was performed. The tomogram clearly reveals the site's internal structure, with low resistivity areas (warm-colored zones)

371 indicating the relative positions of the infrastructure elements (elevator and galleries on both
372 sides). It also shows the extent of the active layer (moderate resistivity areas near the surface),
373 as well as the permafrost evidenced by high resistivity areas (represented in cool colors).
374 Although the lower part of the tomogram appears similar on both the NW and S profiles, which
375 is expected since they lie in rockwalls that are alike regarding slope and aspect (where the
376 lowest part of the S profile is deployed on the NW face as well, see Fig 1c), significant
377 differences are evident in the upper part (*i.e.*, above the gallery level). These differences
378 highlight the contrast between the sun-exposed S face, composed of fractured granite (clearly
379 visible in the field; see Fig. 1d) and exposed to strong insolation, leading to drier surface
380 conditions and consequently higher electrical resistivity. In contrast, the shaded NW face
381 mainly consisting of massive granite and less influenced by atmospheric heat flux, remains
382 wetter and thus leads to lower resistivity close to surface. The upper part of the profile therefore
383 reveals strong thermal gradient typical of high-alpine summits (Noetzli et al., 2007; Magnin et
384 al., 2017). The high-resistivity area thus appears limited, likely due to the heat flux from the
385 sun-exposed and warm face towards the close shaded-face.
386
387
388
389

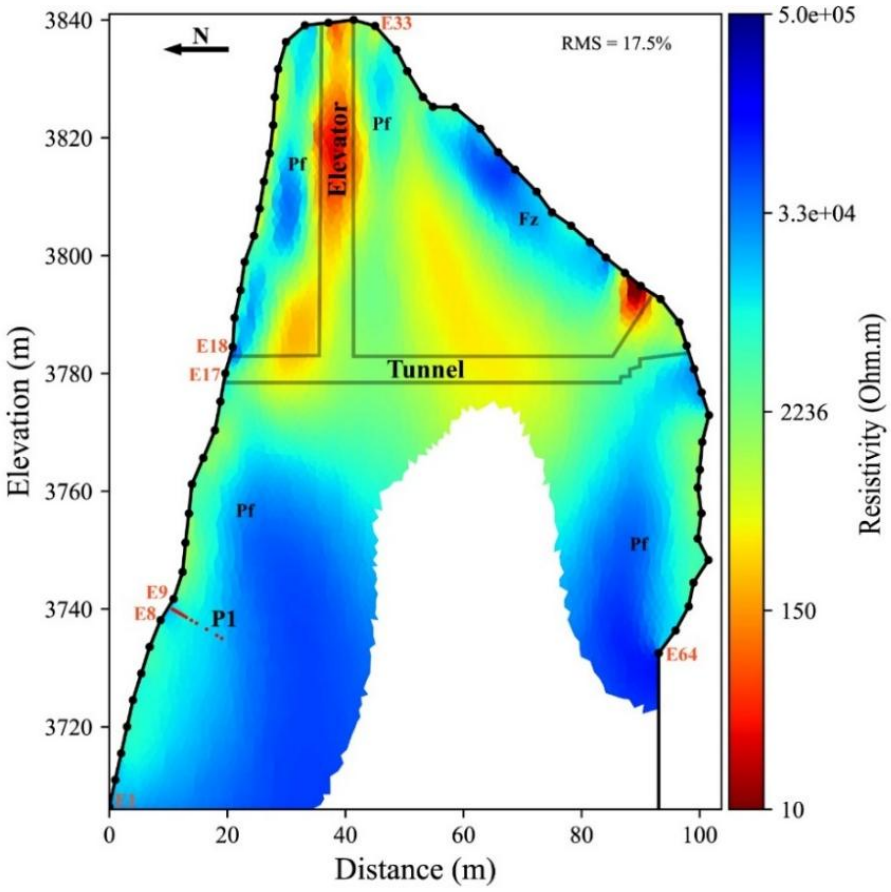


**Figure 5.** Electrical resistivity tomogram over the NW+S profile measured on August 26, 2020. A total of 320 data points used for the inversion (475 data points constitute the complete pseudo-section), about 30% of dataset was filtered). Grey lines indicate the approximative positions of infrastructure (galleries and elevator). Pf stands for Permafrost zone and Fz for Fractured zone. E1 to E64 are Electrode numbers. Red dots at P1 indicate positions of the thermal sensors in BH-NW.

Figure 6 provides an example of the resistivity tomogram for the combined NW and E profiles. This tomogram highlights the changes in resistivity associated with permafrost, active layer, and anthropogenic installation (such as the elevator and gallery (relatively far from the profile at the E side compared to S profile)). On the eastern side, a thick and desiccated active layer (> 5 m depth) is observed, with some resistive zones near the surface. Indeed, these resistive zones are likely fractured zones creating an unsaturated and air-filled zone and surrounded by moderate resistivity regions where fractures are filled or where water drainage is weak or absent.

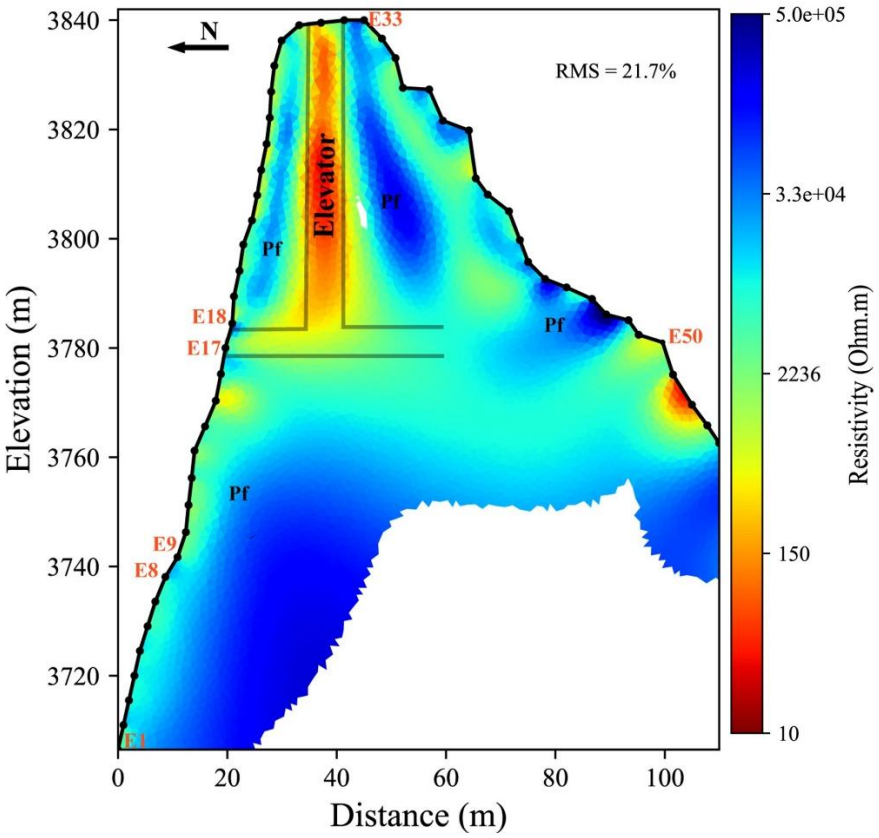


405

406 **Figure 6**. Electrical resistivity tomogram over the profile NW+E at the end of summer (September 25
407 th, 2021). A total of 310 data points were used for the inversion (475 data points constitute the complete
408 pseudo-section), about 35% of dataset was filtered). The last 10 electrodes from the E profile were
409 removed during processing due to connection issues. Pf stands for Permafrost zone

410

411 **5.3. Seasonal and interannual variations**

412 In order to track the seasonal and interannual variations in the permafrost, a time-lapse
413 inversion approach was employed to invert datasets for each profile (NW, S), while the data at
414 the east profile was excluded from this analysis due to significant data gaps caused by poor
415 electrical connection and cable malfunctions. Figure 7 shows the tomograms of resistivity
416 distribution after a time-lapse inversion of selected datasets acquired along the NW profile at
417 different time intervals. A more complete times series is presented in appendix D, while the
418 results from the south profile are discussed in section 5.6. Spatial and temporal changes in
419 resistivity can be observed, while the anomaly related to the gallery (the warm-colored area

(low resistivity area)) remains relatively consistent over time. The permafrost layer associated with high resistivity, is observed in two zones, above and below the gallery. 2021 was, on average, cooler than both 2020 and 2022 in coherence with air temperature (Fig. 2), and this is reflected in the tomograms by a more prominent cool-colored zone (indicating colder conditions) in 2021 compared to data in 2020 (Fig. 7b and d). Additionally, there is a significant variation in the lower part of the tomograms in 2022 (Fig. 7e), which may be related to water infiltration in fractures that shortcut the heat transfer from the surface to depth (Hasler et al., 2011). However, this area is uncertain, as it is located at the border of the tomogram where sensitivity is low. In addition, the RMS error is high in this tomogram, indicating high uncertainties. Therefore, this information should be carefully considered and verified with further measurements focused on the zone of interest. Unlike Offer et al. (2025), no evidence of water pressurization was observed from the geophysical measurements on the NW face. This is most likely due to the distance between the monitored area and the water table laying at about 1000 m lower (Magnin and Josnin, 2021), and that leads to water drainage.

Instead of analyzing temporal resistivity changes in absolute terms, Figure 7 (f - i) illustrates the resistivity variation ratio between two subsequent measurements. This approach facilitates the tracking and visualization of small changes in resistivity. A value of 1 (represented in white color) corresponds to no change in resistivity between the two measurements (reflecting consistent thermal/hydrological conditions over time), while the blue color indicates that the resistivity increased over time, and the red color represents the inverse. It can be observed that seasonal variations are the most pronounced, as illustrated in Figure 7g, h and i, compared to short-term fluctuations (see Fig. D2). The effects of freezing and thawing are marked by maximum variations near the surface (in the active layer). In contrast, over a short time interval (*i.e.,* a few weeks), only minor variations are noted (*e.g.*, Fig. 7f, Fig. D2 b, e and j). The decrease in resistivity near the surface at approximately 3780 m, observed in

445 Figure 7i, could be related to water flow around the gallery, where water circulation and
446 percolation in the galleries occurs every summer (Ben-Asher et al., 2025). Consequently, a
447 specific water diversion system has been installed to protect tourists from these water flows.
448 Furthermore, at approximately 3740 m, close to borehole BH-NW, we observe variations in
449 resistivity, with values higher than in the surrounding zone, forming a vertical pattern visible in
450 Figures 7b, d, and e. These features coincide with open sub-vertical fractures that affect the
451 temperature-depth profile in boreholes (Magnin et al., 2015).
452

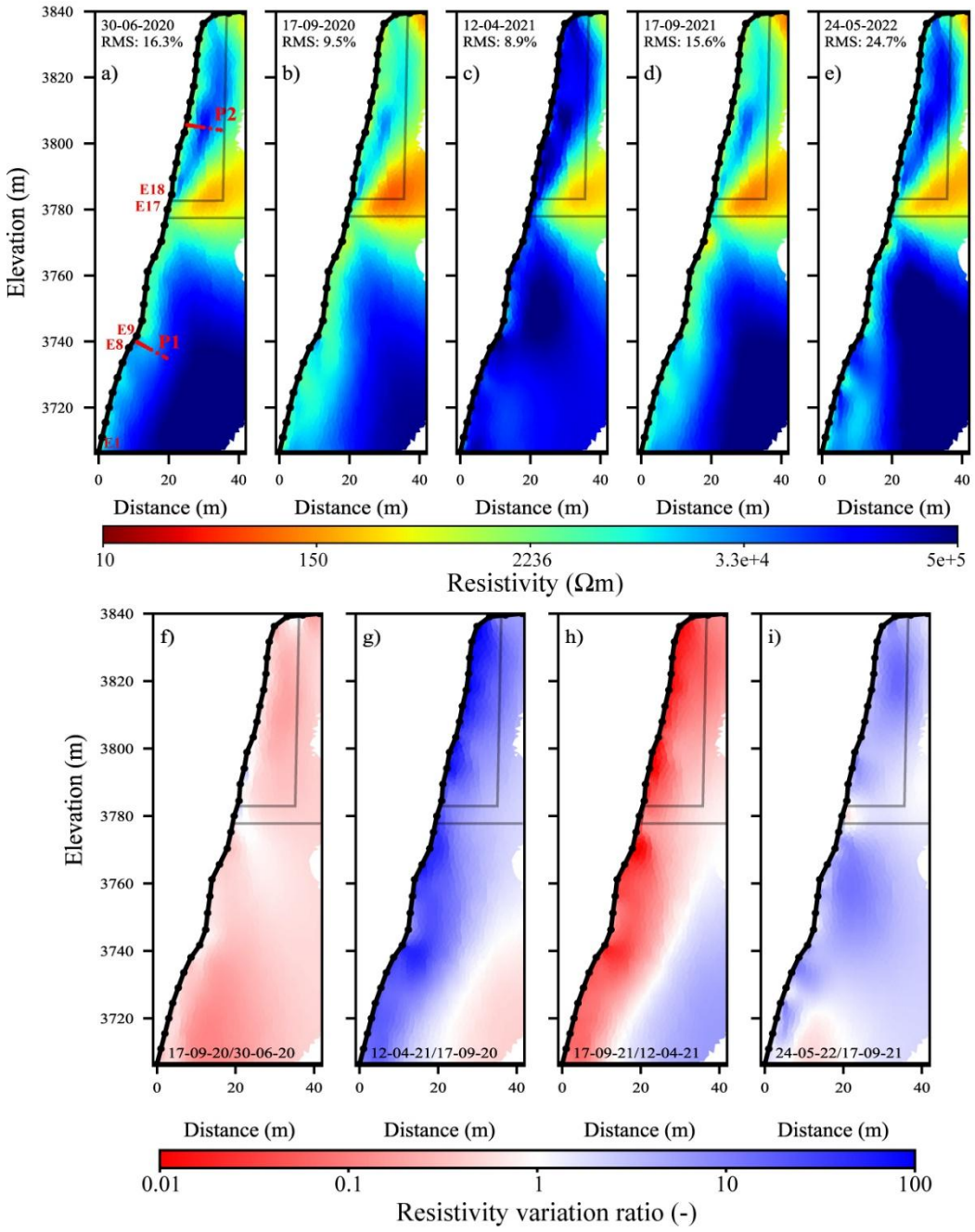


**Figure 7.** Seasonal and interannual variations of electrical resistivity at NW side. a - e) electrical resistivity tomograms at different dates (from June-2020 to June-2022). The conductive zone (in warm colors) denotes the presence of the gallery and elevator (see Fig. 5). The red dots (P1 in panel a) indicate the positions of the thermal sensors in the borehole BH-NW. Data presented on Figures 8, 10 and 11 are extracted at the red dots (P1 and P2). f - i) resistivity variation ratio between consecutive electrical resistivity tomograms. Blue colors indicate an increase in resistivity, while red colors represent a decrease in resistivity from one measurement to the next.

463 **5.4. Virtual borehole analysis**

464 Inverted resistivities were extracted along profiles P1 and P2, corresponding to borehole
465 BH-NW and a virtual borehole, respectively (see positions of P1 and P2 in Fig. 7a). The
466 extracted resistivities (Fig. 8) show that the variation of resistivity with depth is more
467 pronounced at P2 than at P1. This greater variation could be due to a higher water content in
468 the active layer or a thicker active layer at P2 compared to P1. The greater thickness of the
469 active layer in the upper section can be explained by the 3D heat transfer and the proximity of
470 the shaded face (NW side) to the sun-exposed faces (S side) in the top part (Magnin et al.,
471 2017), as well as the greater amount of direct sun-beams at the summit than in the more shaded
472 lower parts of the face. The 3D effects are well visible at depth of P2, where resistivity decreases
473 due to warmer conditions close to the opposite sun-exposed face. In the lower section at P1, the
474 contrast between the resistivity in the active layer and that in the permafrost is not significant.
475 This may be attributed to (i) reduced thermal variability because of snow accumulation in this
476 zone (see Fig. 1c), where the snowpack acts as a thermal insulator, reducing temperature
477 variability; (ii) the presence of fractures (as noted above) influencing the temperature-depth
478 profile (see Fig. 7b, e and d). However, it is important to note that the ALT is about 2.7 m at
479 the end of summer (based on BH-NW measurements; see Fig. A1), whereas, the smallest
480 quadrupole spacing is 15 m, leading to effective depth around 2.55 m (Edwards, 1977), which
481 is insufficient to fully capture the resistivity variations near the surface. Additionally, a slight
482 decrease in permafrost resistivity is observed between 30 June 2020 and 30 June 2022. That is
483 consistent with the observed permafrost warming at 10 m depth (Magnin et al., 2024). Finally,
484 in 2021, resistivity values were higher in both the upper and lower parts (at P1 and P2)
485 compared with 2020 and 2022, consistent with the temperature measurements (see Fig. 2, or
486 details in Magnin et al. (2024)).

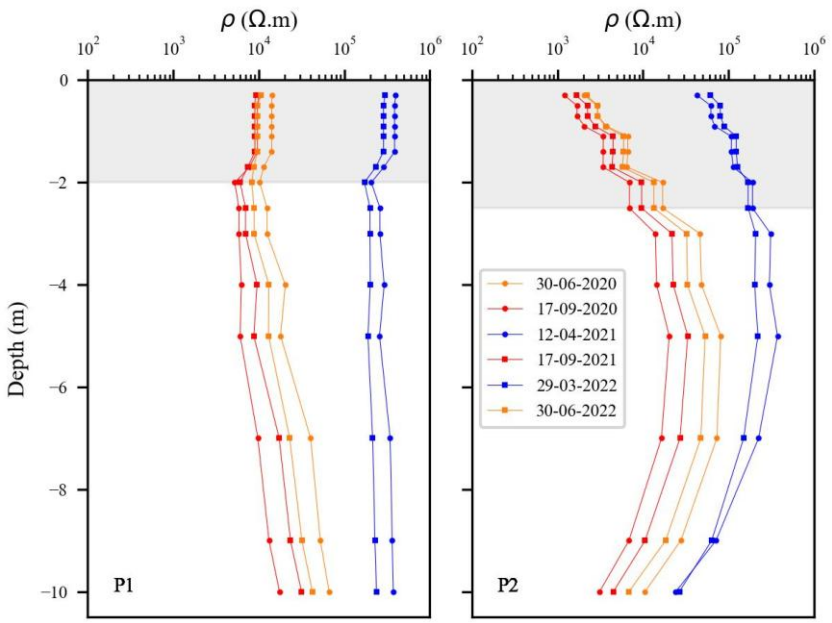


**Figure 8.** Resistivity extracted over depths at different dates and locations (P1, P2). Resistivities are extracted from tomograms in Fig. D1. There is greater variation at the higher profile (P2), where heat transfer from the nearby sun-exposed faces is more significant in the site's upper part.

## 5.5. Temperature - resistivity relationship

Figure 9 presents the measurement results for the granite sample from the study site (labeled Sample AdM), alongside measurements of another granite sample (Sample Cosmiques) collected from a nearby site at the lower Cosmiques Ridge (Mont-Blanc massif, 3613 m a.s.l.), as reported by Duvillard et al. (2021). The experimental datasets are presented along with data fits, using Equations 1 for temperatures above the freezing point, and Equation 2 for temperatures below the freezing point. The model proposed in Section 3 successfully fits the data above and below the freezing temperature, providing a proxy for connecting electrical conductivity or electrical resistivity measured in field to temperature.

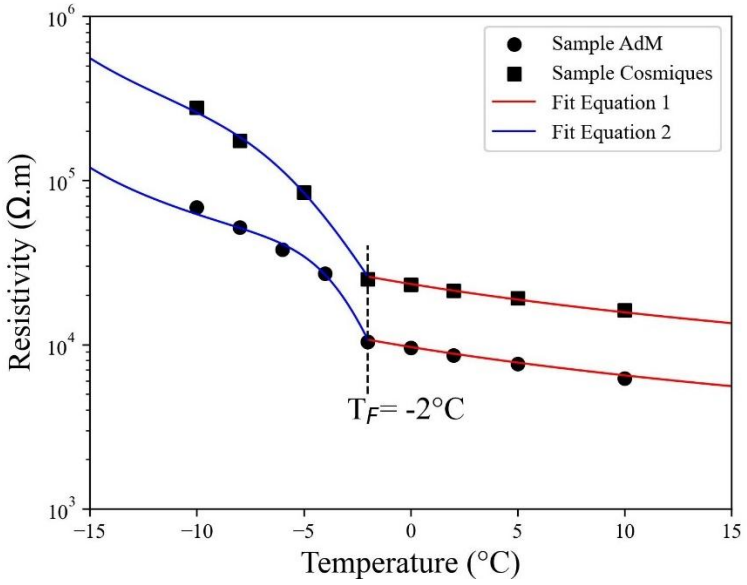


**Figure 9.** Resistivity-temperature relationship from laboratory measurements on two granite samples from (1) the study site (Sample AdM), and (2) from the Cosmiques ridge, Mont-Blanc massif, West (3613 m a.s.l.) (Sample labeled Cosmiques). $T_F$ denotes the freezing temperature. The solid lines correspond to the fits using the Equation 1 (red lines) and Equation 2 (blue lines), in unfrozen and frozen conditions, respectively. The parameters of the model in Equation 2 are ($T_C$=-1.3 °C, $\theta_r$=0.004, $\sigma(T_0)$ = 2.3×10$^{-4}$ S m$^{-1}$) for Sample AdM, and ($T_C$= -2.17 °C, $\theta_r$ = 0.004, $\sigma(T_0)$ = 9.5×10$^{-5}$ S m$^{-1}$) for Sample Cosmiques.

Extracted resistivities at P1 are superimposed on the co-located borehole BH-NW, where temperature measurements are available. We are using these two datasets (*i.e.*, temperature and resistivity measurements at the same location, BH-NW) to explore the potential for estimating temperature based on electrical resistivity measurements and to perform a quantitative evaluation of the temperature - resistivity relationship determined in a laboratory.

It is well established that when temperature > 0 °C (*i.e.*, the case in the active layer), electrical resistivity depends on multiple factors, including porosity, water content, water salinity, Cation Exchange Capacity (CEC) and temperature (Revil et al., 2018). This multiple parameter dependance makes it difficult to accurately model or predict electrical resistivity, or to use it as a proxy for temperature estimation in the active layer. In contrast, under frozen conditions, resistivity of the medium is primarily controlled by the remaining unfrozen pore

522 water, which is largely temperature dependent, while other parameters can be assumed
523 relatively constant.

524 Based on this assumption, the resistivity values extracted from inverted model of
525 resistivity were converted to temperature using the petrophysical model in Equation 2
526 (Duvillard et al., 2021; 2018; Coperey et al., 2019). Figure 10 shows the measured temperature
527 alongside the estimated temperature from ERT data, plotted against depth at different dates (in
528 summer and autumn). A good agreement is observed between the measured and estimated
529 temperature in frozen zone, with mean absolute error (MAE) less than 1 °C within the frozen
530 zone (approximately from 2-2.5 m to 10 m, depending on the date). These results suggest that
531 the temperature distribution across the site can be reasonably estimated using this model,
532 assuming that the medium is sufficiently homogeneous and that resistivity variations are
533 predominantly controlled by temperature. Figure 11 illustrates the temperature distribution
534 along the profile NW estimated from electrical resistivity measurements acquired at different
535 dates between June 2020 and June 2022. The estimated temperatures consistent with previous
536 analyses and highlight two permafrost zones located above and below the gallery. A clear
537 temperature gradient with depth is observed on the 2D temperature sections, with positive
538 temperatures around and in the infrastructure. It can also be observed that temperature decreases
539 with depth, reaching values lower than -5 °C in the zone where ERT sensitivity is low or absent
540 (see lower part of profile NW Fig 11). At greater depths, the reduced sensitivity affects the
541 reliability of temperature estimates.

542 Finally, data collected under frozen surface conditions (*i.e.*, measured in winter and
543 early spring, when contact resistance is high) shows large discrepancy between the estimated
544 and measured temperature and therefore cannot be reliably used for temperature estimation.
545

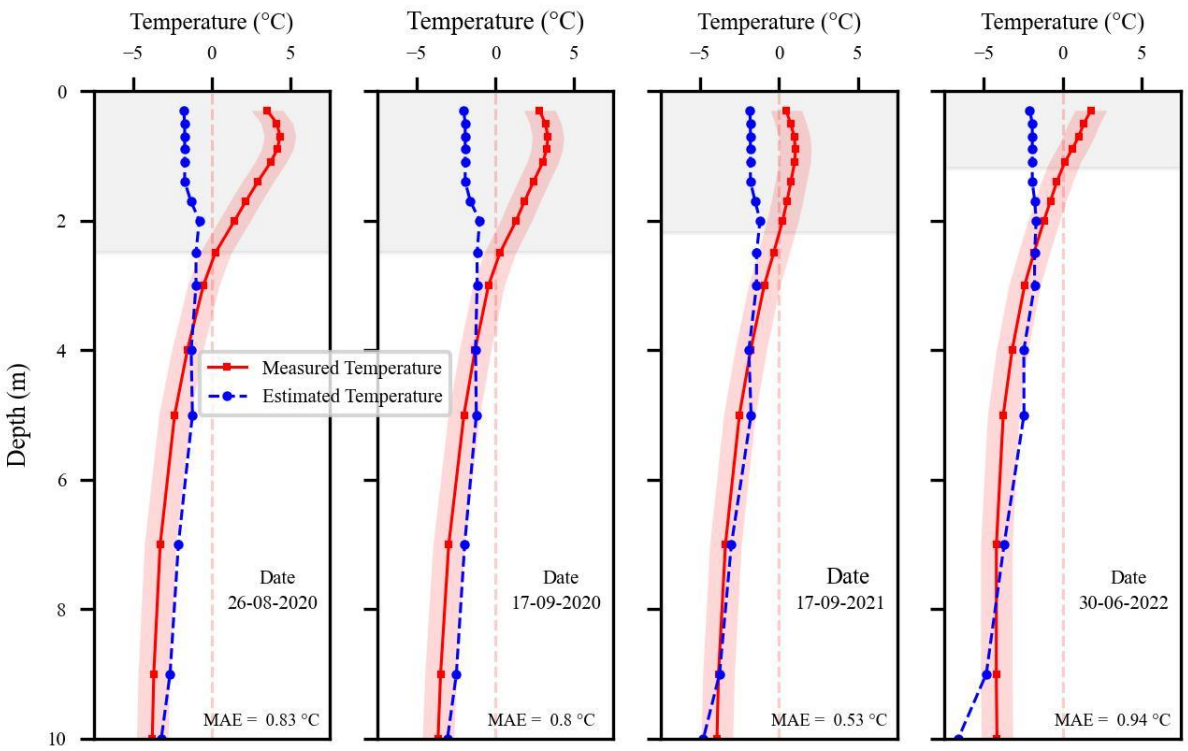


546

547 **Figure 10.** Comparison between measured temperatures in BH-NW and estimated temperatures derived
548 from geophysical measurements (*i.e.*, extracted resistivity values at different dates) using the
549 petrophysical model in Equation 2. The gray-shaded area indicates the extent of the active layer at the
550 time of measurement. The red-shaded zones show the ±1 °C range around the measured temperature.
551 The mean absolute error (MAE, in °C) quantifies the average error within the frozen zone for each date.
552

553

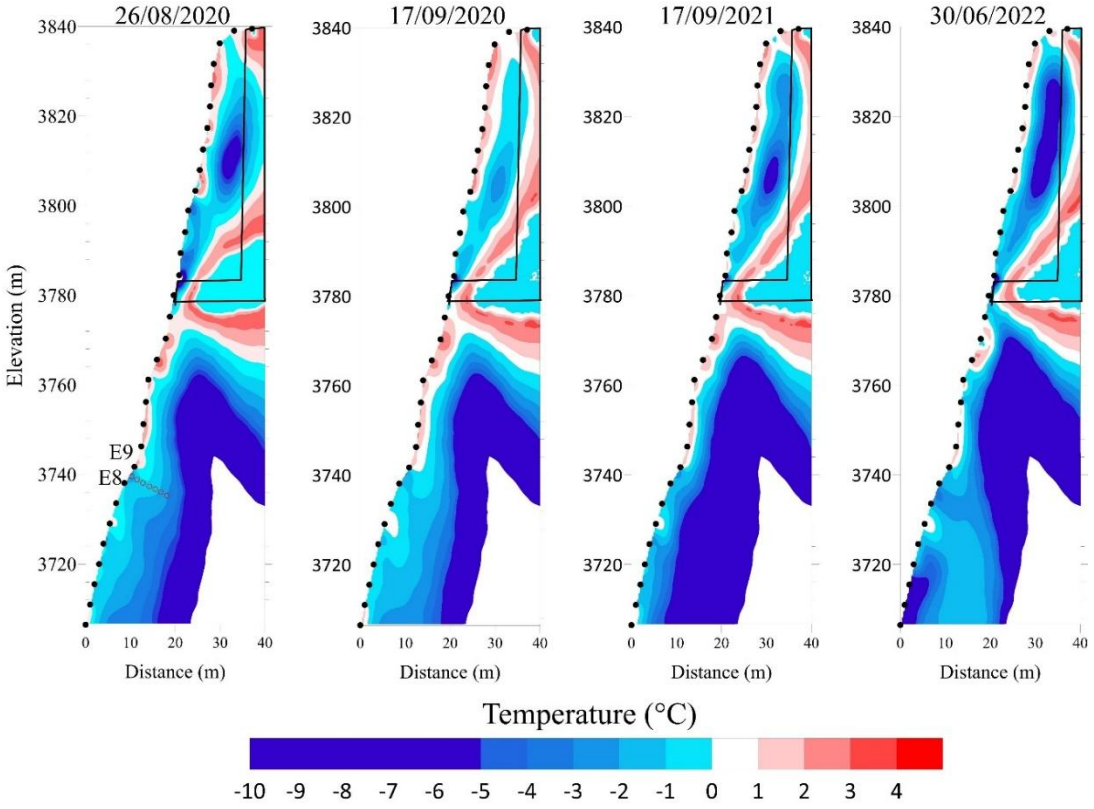


**Figure 11**. Spatio-temporal evolution of subsurface temperatures along the NW profile derived from electrical resistivity measurements, using Equation (2) and parameters obtained from laboratory measurements. Black dots indicate the electrode positions. The red circles indicate the location of borehole BH-NW, while the black lines mark the relative positions of the gallery and the elevator. The blanked zones in the lower part of the profile correspond to areas of low sensitivity of the geophysical measurements and are therefore not reliable to temperature estimation.

To go further in our analysis, Figure 12 shows the extracted resistivity at P1 vs. temperature data measured in co-located BH-NW at different dates. Laboratory measurements on two granite samples (labeled Sample AdM and Sample Cosmiques) are also shown. Three key observations can be made: i) Data collected in winter and spring (frozen conditions at surface), presented by blue symbols, show resistivity values higher than those expected from laboratory measurements, which aligns with the field observations reported by Maierhofer et al (2024). This may be related to the salt segregation during freezing, which may enhance

conductivity of pore water and consequently reduce resistivity of samples. ii) At higher temperature (unfrozen conditions at surface), a linear trend is observed that aligns with laboratory measurements for part of datasets (e.g., datasets of 26/08/2020 and 17/09/2020). The difference in resistivity between field and laboratory data under unfrozen conditions could be attributed to the heterogeneity at the field scale and/or the difference in water content and water salinity between laboratory and field environments. Whereas laboratory measurements were conducted in saturated conditions (saturation was performed under vacuum using degassed water). iii) Field data exhibit greater dispersion compared to laboratory data, which can be attributed to several factors, including 3D effects at the site, the influence of infrastructure and heterogeneity at different scales (from fractures scale to pore scale). In addition, there is a difference in resolution between the two field measurements: temperature measurements are local, while resistivity measurements account for a larger volume.

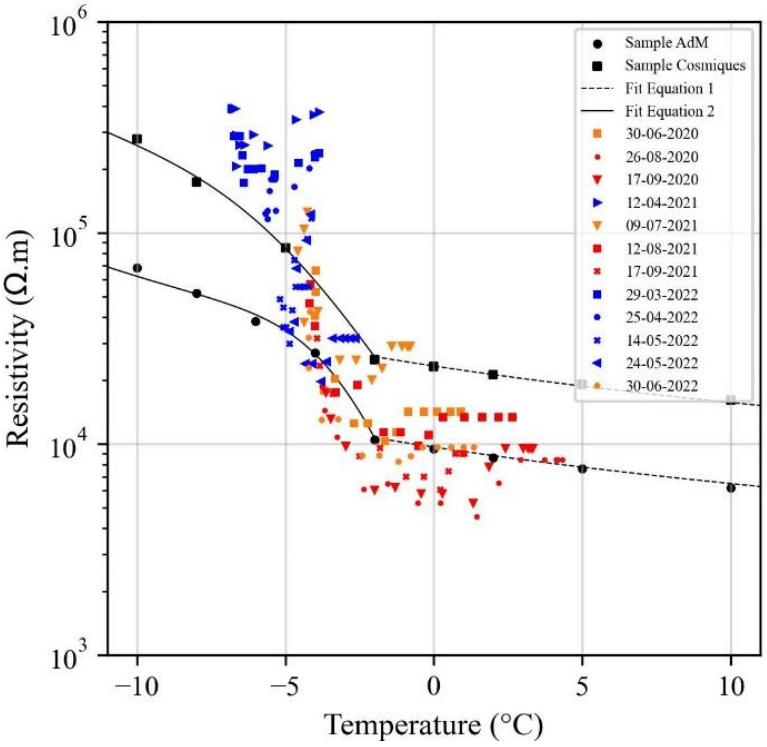


**Figure 12.** Resistivity vs. temperature. Resistivities are extracted from the tomograms in Figure D1 at location P1. Temperature is measured by sensors at BH-NW. Laboratory data on two granite samples and fitting with Equation 1 and 2 are shown too.

## 5.6. Hydrogeological dynamics

One of the objectives of this study was to assess hydrogeological dynamics. Due to gaps in the ERT time series, the analysis of times series did not yield conclusive information. Therefore, we selected specific datasets (nearly complete pseudo-sections) and compared the results of the time-lapse inversion to gather information about water infiltration and drainage. Although we could not precisely identify the infiltration and drainage pathways or the water table (which may be located at a lower altitude according to Magnin and Josnin (2021)) using ERT measurements, we observed several instances that serve as evidence of possible water flows.

Figure 13 shows the results of the time-lapse inversion of datasets along the S profile at various time intervals. The same inversion parameters were applied as those used to invert the datasets on the NW side (Fig. 7). In the upper part of the profile (*i.e.,* above the gallery), we interpret that seasonal variations in resistivity are influenced by the presence of fractures, which control water flow pathways and, consequently the resistivity response throughout the seasonal cycle. This portion of the profile is exposed to strong insolation in summer, which dries the rock and fractures, leading to an increase in resistivity near the surface due to air-filled pores and fractures (*e.g.*, Fig 13b, c and l). Conversely, decreases in resistivity in this zone (*e.g.*, Fig 13a, d and g), can be attributed to higher water saturation caused by the circulation of snowmelt or rainfall water. Snowmelt on this side supplies substantial amounts of water throughout the thawing season (Ben-Asher et al., 2023). The conductive zone observed beneath the desiccated area (*e.g.*, Fig. 13d and h) likely corresponds to zone of increased water saturation, as also reported by Sass (2004).

In the lower part of the S profile (*i.e.*, below the gallery), the seasonal variations in permafrost resistivity are clearly observed and can be tracked over time, with no evidence of significant water flow or drainage in this zone. This portion of the S profile shares a similar sun

exposure to the NW profile and therefore exhibits comparable dynamics, with the development of a thawed and more water saturated active layer than in the upper part, because it is less exposed to solar radiation, and it undergoes less desiccation than the south face sector.

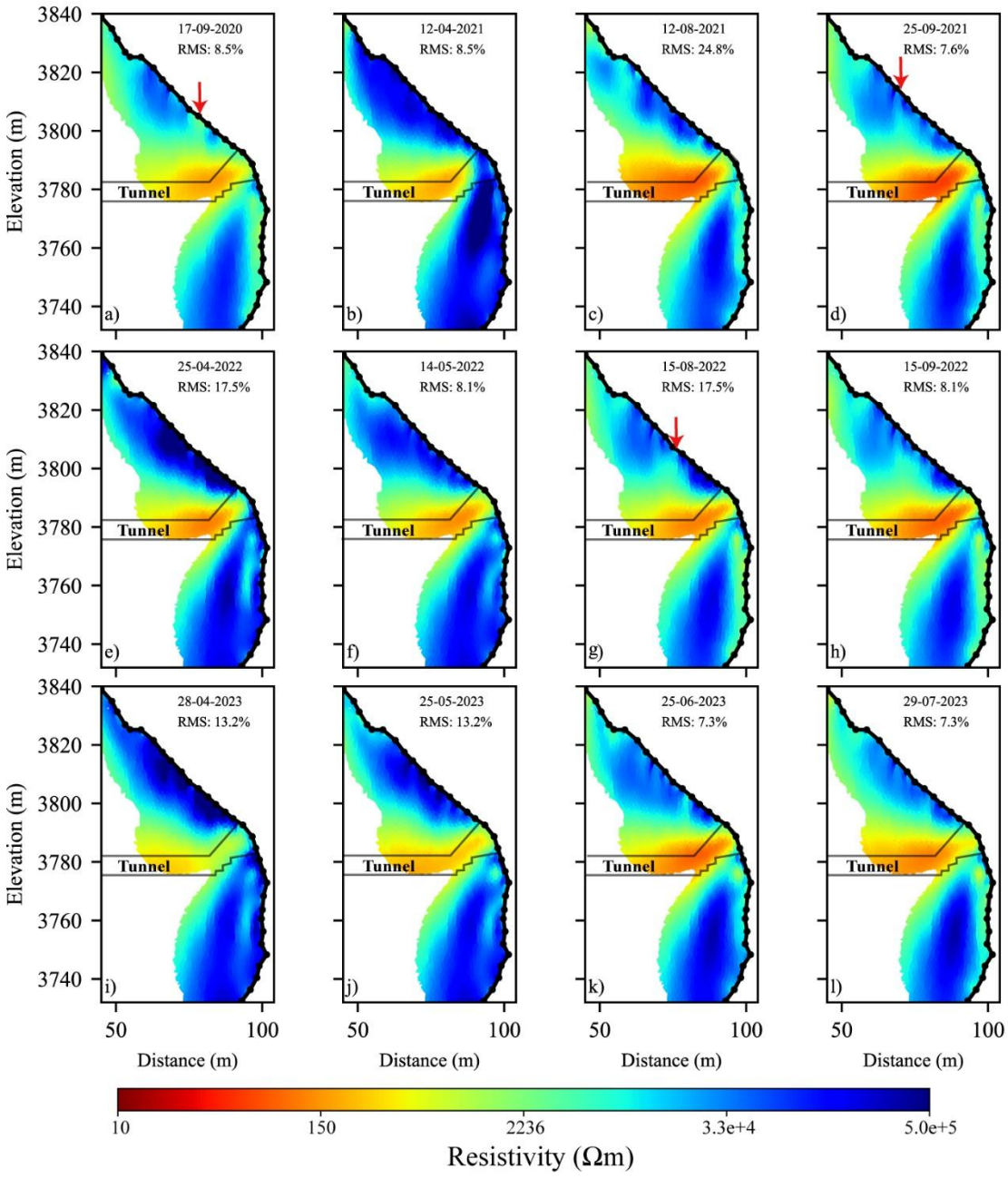


**Figure 13.** Tomograms of resistivity along the south side (S profile). Electrical resistivity tomograms at different dates (from September-2020 to July-2023). The conductive zone (in warm-colors) explained by the presence of the gallery. The red arrows indicate the potential zones of water infiltration from snowmelt or precipitation.

# 6. Discussion

In this study, we use repeated and automated ERT to investigate the evolution of permafrost at a high altitude rockwall site. As expected, data from A-ERT are of lower quality compared to manual measurements, where the operator can intervene to improve CR after each electrode check (Doetsch et al., 2015; Hilbich et al., 2009). High CR is the main challenge preventing the year-round collection of high quality data at high altitude rockwall sites such as the site investigated in this study. Therefore, conducting ERT in frozen surface conditions on rockwall permafrost remains challenging because of the high CR. Various approaches were tested to improve CR. For instance, duplicated electrodes provided a durable and significant improvement in CR (~ one order of magnitude reduction), helping to enhance data quality.

Time lapse inversion of the measured resistivity showed the seasonal and interannual variations (Fig. 7, 8 and 13). We observe that resistivity decreased over time at greater depths (*e.g.,* at P1 and P2, comparing data from July 30, 2020, and July 30, 2022), indicating degradation of the permafrost as also revealed by borehole measurements (Magnin et al., 2024). However, this decrease in resistivity is minor, likely due to the relatively short observation period of two years at NW side and four years at S side. A thicker active layer is observed at the upper section, which can be attributed to 3D heat transfer processes and the close proximity of the shaded north-west face to the sun-exposed southern faces in the upper part of the slope (Magnin et al., 2017; Noetzli et al., 2007).

The contrast between the resistivity in the active layer and that in permafrost is not significant in the lower section on the NW side at BH-NW (P1 Fig. 8), which may result from low ice content/water content where the porosity is around 1 %, the insulating effect of snow accumulated in the zone of the BH-NW or due to high surface conductivity in granite. The alteration of granite involves the transformation of primary minerals (mica and alkali feldspars) into secondary clay minerals (such as kaolinite), which are known for their high cation

exchange capacity and, consequently, their contribution to surface conductivity (Piolat et al., 2025; Revil et al., 2024). Additionally, the sensitivity of the used electrode array (with a smallest quadrupole length of 15 m) could affect the resolution of ERT image near the surface (Binley and Kemna, 2005).

One of the objectives of this study was to evaluate the potential of using field resistivity measurements to provide 2D or 3D information on thermal distribution in permafrost, based on the superposition of resistivity and temperature datasets. The temperature estimation based on ERT data leads to good agreement with observed temperatures, with a mean absolute error of less than 1 °C at depths between 2.5 to 10m, indicating that the proposed model (Equation 2) can reasonably reproduce subsurface permafrost temperatures. Consequently, this approach can provide valuable insights into the site's thermal distribution as shown in Figure 11, even though internal permafrost temperatures typically lie just a few degrees below freezing (e.g., Noetzli et al., 2024). However, a precision of ±1 °C may be insufficient in permafrost studies, where minor temperature variations can greatly impact stability and long-term thermal evolution. Nevertheless, this level of accuracy remains within the uncertainty range commonly reported for thermal models (Magnin et al., 2017).

On the other hand, predicting temperature in the active layer remains challenging, as temperature is not the dominant factor affecting resistivity in thawed conditions. Data collected under frozen surface conditions (*i.e.*, measurements taken in winter and spring with high contact resistance) resulted in larger discrepancy between estimated and measured temperature and could not be reliably used for temperature estimation. Consequently A-ERT measurements remain challenging when the ground surface is frozen, mainly due to the high contact resistance.

Furthermore, the transition between frozen and unfrozen conditions is not clearly distinguished at resistivity - temperature curve extracted from field measurements (see Fig. 8, 10). The freezing point, which is expected to result in a significant change in resistivity (as

observed in laboratory measurements), does not exhibit the same effect in field. However, some datasets (e.g., datasets of 12/08/2021 and 17/09/2021) show progressive increase in resistivity when temperature decreased (*i.e.,* indicating progressive freezing). This point needs to be addressed in further research with a smaller electrode array to improve the resolution of geophysical measurements.

On the sun exposed face, the tomograms of resistivity show near-surface pore desaturation, attributed to strong insolation on the rock face that is perpendicular to the sun beam, along with features that may relate to water infiltration along fractures. The exact pathways of infiltration and drainage are still ambiguous, possibly due to the resolution of resistivity measurements. With the AdM setting, we can also hypothesize that the saturated conditions are almost never reached. There is water circulation, but no pressurization or development of a water column, because the water table is likely lower than the area covered by the measurements (Magnin and Josnin, 2021), conversely to Offer et al. (2025) at the Kitzsteinhorn for example. Indeed, our investigation is in a different setting: high altitude peak lying ~1000 m above the water table (Magnin and Josnin, 2021) while in the Kitzsteinhorn outcrops from a glaciated areas with a probably much closer water table.

Finaly, A-ERT acquisition using smaller electrode array can improve near surface resolution and provide more detailed information about the subsurface. Combining ERT with other geophysical methods, such as induced polarization and/or refraction seismic tomography, can also provide complementary petrophysical and spatial sensitivity, enabling a more comprehensive investigation of the hydrogeological system of high mountain permafrost.

## 7. Conclusions

We used repeated and Automated Electrical Resistivity Tomography (A-ERT) to monitor permafrost dynamics over nearly four years at AdM in the French Alps, aiming to

696 better understand the complexities of permafrost behavior in response to climatic variations and
697 to explore the potential of the method for quantitative monitoring. The key findings are
698 summarized as follows:

699 1. Through detailed analyses of ERT data, we were able to characterize the active layer
700 dynamics and identify significant seasonal and multiannual changes in permafrost
701 evolution. Importantly, we observed that the ALT and permafrost conditions below
702 varied significantly from one face to another in coherence with climate signals and
703 measured temperatures in boreholes.
704 2. This research demonstrates that temperature can be quantitatively derived from
705 geophysical measurements of electrical resistivity based on a petrophysical model
706 connecting resistivity to temperature with precision of approximately ±1 °C in
707 frozen granite during summer and autumn monitoring.
708 3. Our assessments of the hydrogeological system revealed instances of possible water
709 flow as well as bedrock desiccation under strong insolation. That said, the exact
710 pathways of infiltration and drainage remain unclear.
711 4. The results underscore the utility of ERT as a promising, non-invasive approach for
712 quantitative monitoring non-linear permafrost evolution in high mountains.

713 Although installation of A-ERT system is relatively low costs, it can require substantial
714 maintenance in high-risk areas like unstable high mountain rockwalls where rockfalls and
715 lightning effects can damage equipment. This study highlights the urgent need to address
716 challenges related to climate conditions at high-altitudes that affect device performance and
717 contact resistances, in order to enhance the reliability and durability of continuous A-ERT data
718 collection.

719

720 **Data availability**. Data will be made available on request to the corresponding author.

721 **Author contributions.** FA performed the data analysis, prepared the figures, and wrote the
722 majority of the text. JB contributed to data acquisition, writing, and figure preparation. FM and
723 AR contributed to the design of the ERT survey, as well as data acquisition and discussion of
724 the results. EM, MBA, LR and PAD contributed to the field installation and acquisition, JR
725 conducted and processed the laboratory data, MK contributed to data inversion and discussion,
726 TC provided air temperature data, PAD offered additional information about the site. Finally,
727 all authors actively contributed to the preparation of this version of the paper.
728
729 **Competing interests.** The authors declare that they have no conflicts of interest.
730
731 **Acknowledgments.** This research is part of the ANR WISPER project (ANR-19-CE01-0018)
732 and the Action Plan on Risks from Glacial and Periglacial Origin (PAPROG) from the French
733 Ministry of Ecological Transition, Biodiversity, Forest, Sea and Fishing. The authors
734 acknowledge the following persons who helped with the field work: Antoine Chabas, Bruno
735 Galabertier, Stéphane Jaillet and Raphaël Gallet from the EDYTEM Laboratory, Simon Alesina
736 from the University of Lausanne, Marc Cleriot for help, and Catherine Coulaud from IGE. The
737 authors are also grateful for the Compagnie du Mont-Blanc that provided access to the site and
738 support. Finally, we thank Vincenzo Lapenna and the four anonymous Referees for their
739 constructive reviews, and we are especially grateful to the Editor, Teddi Herring for her
740 valuable comments during the review of this paper.

# Appendix A: Temperature measurements in boreholes on different dates at BH-NW and BH-S

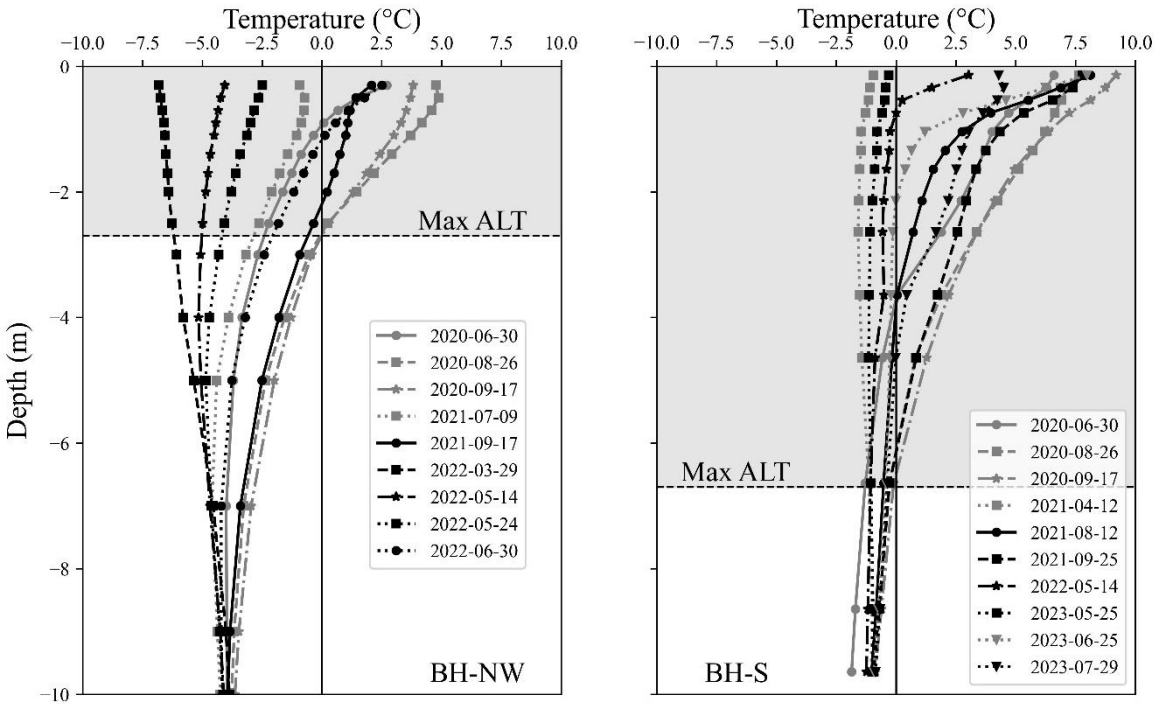


Figure A1: Temperature variation over depth in boreholes BH-NW and BH-S on different dates aligned with the ERT measurement periods shown in Figures 7, 13 and D1. The gray-shaded area indicates the extent of the active layer at each borehole.

748 **Appendix B**: Evolution of the contact resistance (CR) over time at NW and S profiles.

749 The CR measured before each daily measurement between 09/2021 and 12/2023 are presented
750 in Figure B1.

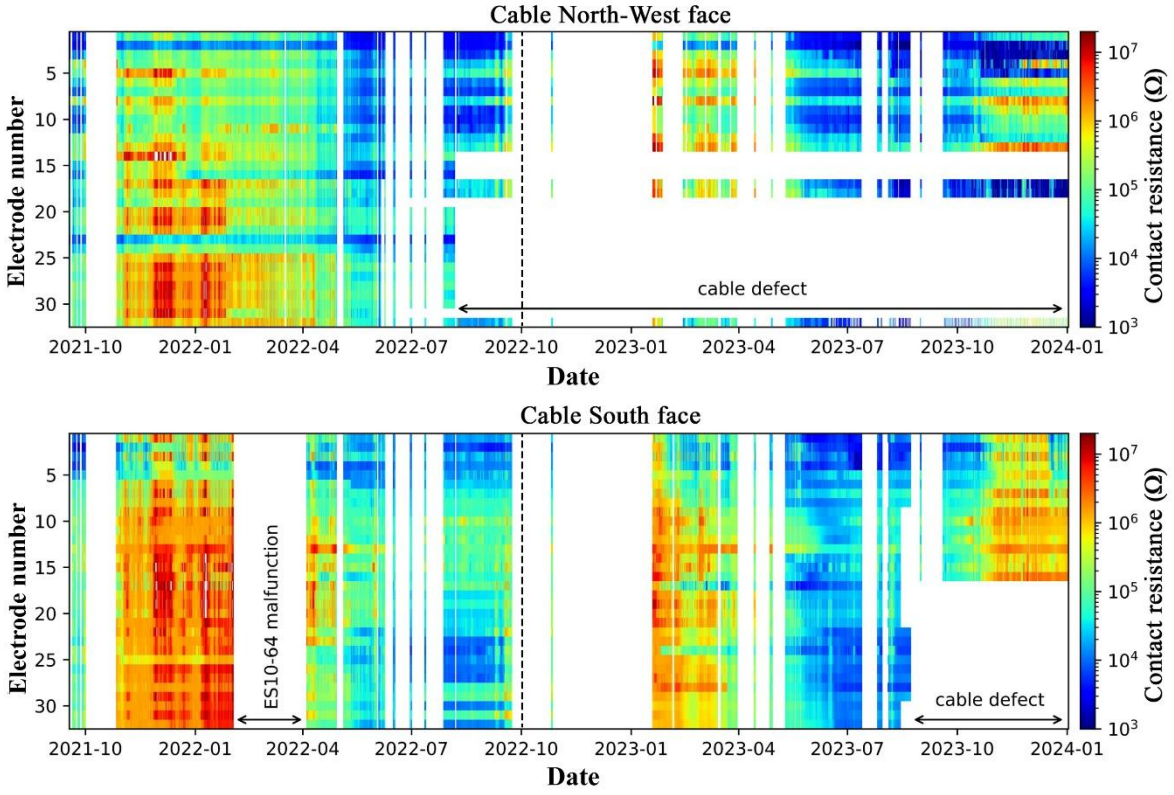


751

752 **Figure B1.** Temporal evolution of contact resistance at the North-West side and South side. Data partly
753 missing is due to cable defects. The vertical dashed line indicates the date at which the duplicate
754 electrodes were installed.

755

# **Appendix C:** Summary of data presented in this study

**Table C1**. Summary of data presented in this study. Number of data before filtering is 155 datum points of Wenner configuration. Most of datasets have more than 80% of total number of measurements. Two datasets have more than 40% of lost data because of disconnected electrodes.

| **Date** | **N-W Profile** | | **S Profile** | |
|---|---|---|---|---|
| | Number of data after filter | Percentage (%) | Number of data after filter | Percentage (%) |
| 30-06-2020 | 151 | 97.5 | - | - |
| 26-08-2020 | 149 | 96.1 | 90 | 58 |
| 17-09-2020 | 151 | 97.5 | 90 | 58 |
| 12-04-2021 | 118 | 76.1 | 121 | 78 |
| 09-07-2021 | 114 | 73.5 | - | - |
| 12-08-2021 | 149 | 96.1 | 140 | 90.3 |
| 17-09-2021 | 145 | 93.5 | 131 | 84.5 |
| 25-09-2021 | 143 | 92.2 | 144 | 92.9 |
| 29-03-2022 | 121 | 78 | - | - |
| 25-04-2022 | 141 | 91 | 131 | 84.5 |
| 14-05-2022 | 141 | 91 | 147 | 94.8 |
| 24-05-2022 | 140 | 90.3 | 146 | 94.1 |
| 30-06-2022 | 102 | 65.8 | - | - |
| 30-07-2022 | - | - | 145 | 93.5 |
| 15-08-2022 | - | - | 145 | 93.5 |
| 15-09-2022 | - | - | 144 | 93 |
| 19-03-2023 | - | - | 138 | 89 |
| 28-04-2023 | - | - | 143 | 92.2 |
| 25-05-2023 | - | - | 148 | 95.5 |
| 25-06-2023 | - | - | 144 | 92.9 |
| 29-07-2023 | - | - | 140 | 90.3 |

# **Appendix D:** Time-lapse inversion results

Appendix D presents time-lapse inversions of a large number of datasets from north-west face and south faces. The Resistivity variation ratio between consecutive electrical resistivity tomograms is also evaluated. A summary of these datasets is provided in Table C1.

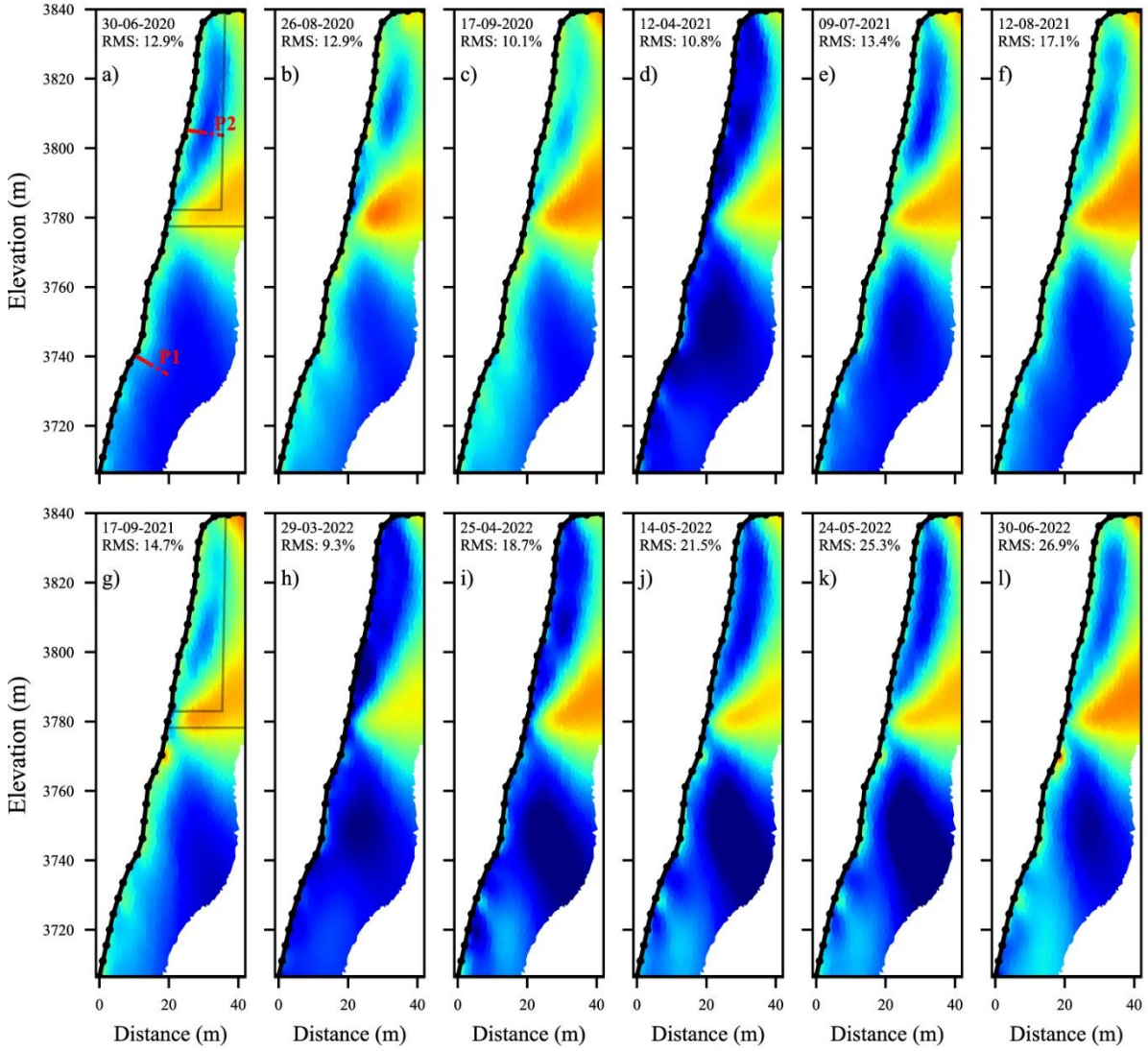


**Figure D1.** Electrical resistivity tomograms at different dates (from June-2020 to June-2022) along the NW side (NW profile). The conductive zone (in warm colors) indicates the approximate position of the gallery and elevator (see Fig. 5). The red dots (P1 in panel a) indicate the positions of the thermal sensors in the borehole BH-NW. Data presented on Figures 8, 10 and 12 are extracted at the position of the red dots (P1 and P2).

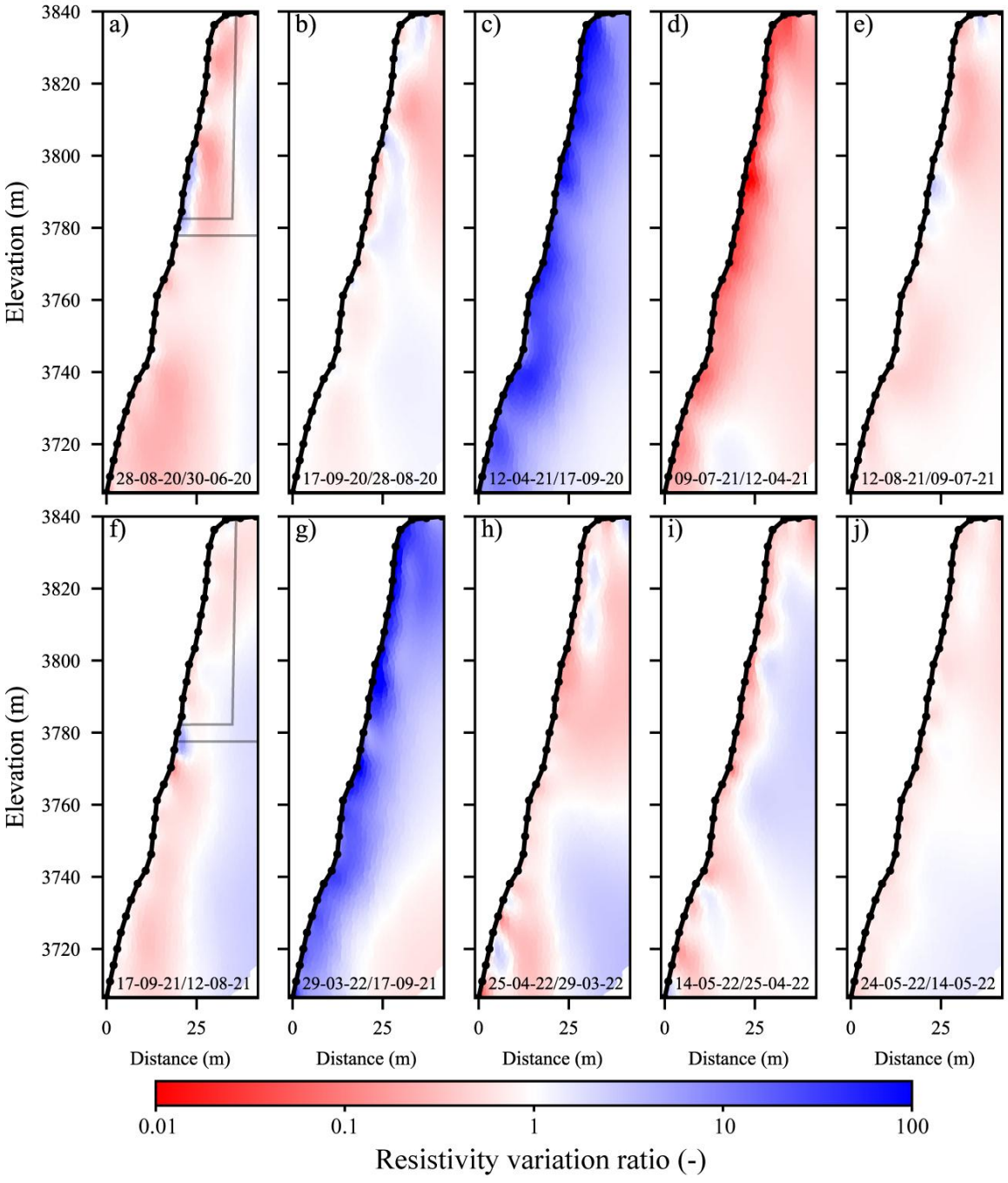


775

776 **Figure D2.** Resistivity variation ratio between consecutive electrical resistivity tomograms (shown in
777 Fig. D1) along the NW side. Blue colors indicate an increase in resistivity, while red colors represent a
778 decrease in resistivity from one measurement to the next.

779

780 Figure D3 illustrates the resistivity variation ratio between successive measurements on
781 the S profile (Figure 13). The dynamics of the active layer are evident, with freezing-thawing
782 effects visible near the surface (*e.g.*, Fig. D3a, d, and g). The heat effect (*i.e.*, decrease in

783 resistivity values near the surface) is more pronounced in the lower section (below the gallery).
784 Another type of anomaly could be observed at greater depth, where heat and/or cool waves
785 resulting from heat transfer (with delay) lead to local variations at greater depth (*e.g.,* Fig. D3,
786 e, g and i). In contrast, the fractured zone in the upper portion obscures the temperature
787 dependency of resistivity due to fluctuations in air and water content (*i.e.*, resistivity in this zone
788 is impacted by factors beyond just temperature). Water infiltration in this area could explain the
789 rapid and significant decrease in resistivity observed between 3790 and 3820 m a.s.l. (*e.g.,* Fig.
790 D3c, f, and j), which increases the thickness of active layer in this zone.

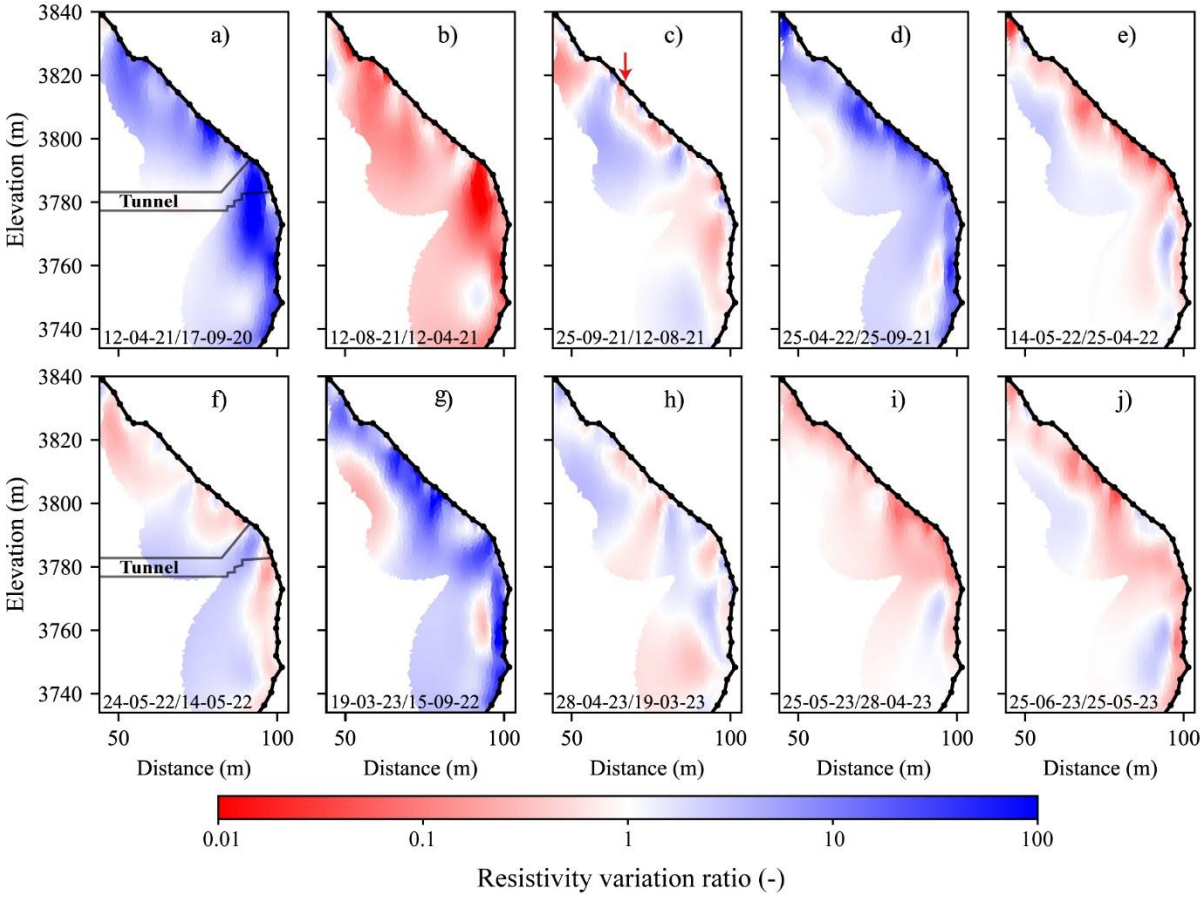


791

792 Figure D3. Resistivity variation ratio between consecutive electrical resistivity tomograms (shown in
793 Fig. 13) along the South side. Blue colors indicate an increase in resistivity, while red colors represent
794 a decrease in resistivity from one measurement to the next. The red arrow shows the position of possible
795 water infiltration inferred from the relative variation compared with the surrounding area.

796

# References

Abdulsamad, F., Revil, A., Ghorbani,A., Toy, V., Kirilova, M., Coperey, A., Duvillard, P. A., Ménard, G., and Ravanel, L.: Complex conductivity of graphitic schists and sandstones. Journal of Geophysical Research: Solid Earth, 124, 8223‐8249. https://doi.org/10.1029/2019JB017628, 2019.

Ben-Asher, M., Chabas, A., Josnin, J.-Y., Bock, J., Malet, E., Poulain, A., Perrette, Y., and Magnin, F.: Water flow timing, quantity, and sources in a fractured high mountain permafrost rock wall, EGUsphere [preprint], https://doi.org/10.5194/egusphere-2025-2450, 2026.

Ben-Asher, M., Magnin, F., Westermann, S., Bock, J., Malet, E., Berthet, J., Ravanel, L., and Deline, P.: Estimating surface water availability in high mountain rock slopes using a numerical energy balance model, Earth Surf. Dyn., 11, 899–915, https://doi.org/10.5194/esurf-11-899-2023, 2023.

Binley, A. and Kemna, A.: DC Resistivity and Induced Polarization Methods, in: Hydrogeophysics, Water Science and Technology Library book series, edited by: Rubin, Y. and Hubbard, S. S.,volume 50, 129‐156, https://doi.org/10.1007/1-4020-3102-5_5, 2005.

Bruel, R., Arthaud, F., Magnin, F., Napoleoni, R., Van Reeth, C., Augé, V., Sagot, C., Fructus, M., Birck, C., Choler, P.: Different temperature responses of mountain rockwalls, soils, and lakes to summer heat waves. Reg Environ Change 26, 34. https://doi.org/10.1007/s10113-025-02517-3, 2026.

Campbell, S., Rosa T. Affleck, Sinclair, S.: Ground-penetrating radar studies of permafrost, periglacial, and near-surface geology at McMurdo Station, Antarctica. Cold Regions Science and Technology, 148, Pages 38-49, https://doi.org/10.1016/j.coldregions.2017.12.008, 2018.

Cathala, M., Bock, J., Abdulsamad, F., Deline, P., Josnin, J-Y., Ravanel, L., Revil, A., Richard, J., Verroust, F., and Magnin, F.: Assessing the role of permafrost in the preconditioning and triggering factors of the September 2020 Crête des Grangettes rockfall (southern French Alps), Géomorphologie: relief, processus, environnement, 30, 3, 171-188, https://doi.org/10.4000/12yqn, 2024.

822 Cimpoiasu, M.O., Kuras, O., Harrison, H., Wilkinson, P. B., Meldrum, P., Chambers, J. E., Liljestrand,
823 D., Oroza, C., Schmidt, S. K., Sommers, P., Vimercati, L., Irons, T. P., Lyu, Z., Solon, A., and
824 Bradley, J. A. High-resolution 4D electrical resistivity tomography and below-ground point sensor
825 monitoring of High Arctic deglaciated sediments capture zero-curtain effects, freeze–thaw
826 transitions, and mid-winter thawing. The Cryosphere, 19, 401–421, https://doi.org/10.5194/tc-19-
827 401,2025.
828 Coperey, A., Revil, A., Abdulsamad, F., Stutz, B., Duvillard, P.A., and Ravanel, L.: Low frequency
829 induced polarization of porous media undergoing freezing: preliminary observations and modeling,
830 Journal of Geophysical Research: Solid Earth, 124, doi:10.1029/2018JB017015, 2019.
831 Dahlin, T., and Zhou, B.: A numerical comparison of 2D resistivity imaging with 10 electrode arrays,
832 Geophys. Prospect., 52, 379–398. https://doi.org/10.1111/j.1365-2478.2004.00423.x, 2004.
833 Doetsch, J., Ingeman-Nielsen, T., Christiansen, A. V., Fiandaca, G., Auken, E., and Elberling, B.: Direct
834 current (DC) resistivity and induced polarization (IP) monitoring of active layer dynamics at high
835 temporal resolution, Cold Reg. Sci. Technol., 119, 16‑28,
836 https://doi.org/10.1016/j.coldregions.2015.07.002, 2015.
837 Draebing, D.: Application of refraction seismics in alpine permafrost studies: A review, Earth-Science
838 Reviews, 155, 136–152, https://doi.org/10.1016/j.earscirev.2016.02.006, 2016.
839 Duvillard, P. A., Revil, A., Qi, Y., Soueid Ahmed, A., Coperey, A., and Ravanel, L.: Three-Dimensional
840 Electrical Conductivity and Induced Polarization Tomography of a Rock Glacier, J. Geophys. Res.-
841 Sol. Ea., 123, 9528‑9554, https://doi.org/10.1029/2018JB015965, 2018.
842 Duvillard, P.A., Magnin, F., Revil, A., Legay, A., Ravanel, L., Abdulsamad, F., and Coperey, A.:
843 Temperature distribution in a permafrost-affected rock ridge from conductivity and induced
844 polarization tomography, Geophys. J. Int., 225, 1207‑1221, https://doi.org/10.1093/gji/ggaa597,
845 2021.
846 Edwards, S. L.: A modified pseudosection for resistivity and IP. *Geophysics*, 42, 1020–
847 1036, https://doi.org/10.1190/1.1440762, 1977.

Etzelmüller, B., Czekirda, J., Magnin, F., Duvillard, P.-A., Ravanel, L., Malet, E., Aspaas, A., Kristensen, L., Skrede, I., Majala, G. D., Jacobs, B., Leinauer, J., Hauck, C., Hilbich, C., Böhme, M., Hermanns, R., Eriksen, H. Ø., Lauknes, T. R., Krautblatter, M., and Westermann, S.: Permafrost in monitored unstable rock slopes in Norway – new insights from temperature and surface velocity measurements, geophysical surveying, and ground temperature modelling, Earth Surf. Dynam., 10, 97–129, https://doi.org/10.5194/esurf-10-97-2022, 2022.

Farzamian M, Vieira G, Monteiro Santos FA, et al.: Detailed detection of active layer freeze-thaw dynamics using quasi-continuous electrical resistivity tomography (Deception Island, Antarctica). Cryosphere.14(3):1105-1120. https://doi.org/10.5194/tc-14-1105-2020, 2020.

Günther, T., Rücker, C., and Spitzer, K.: Three-dimensional modelling and inversion of dc resistivity data incorporating topography-II. Inversion. Geophysical Journal International, Volume 166, Issue 2, August 2006, Pages 506–517, https://doi.org/10.1111/j.1365-246X.2006.03011.x, 2006.

Hartmeyer, I., Delleske, R., Keuschnig, M., Krautblatter, M., Lang, A., Schrott, L., and Otto, J.-C.: Current glacier recession causes significant rockfall increase: the immediate paraglacial response of deglaciating cirque walls, Earth Surf. Dynam., 8, 729–751, https://doi.org/10.5194/esurf-8-729-2020, 2020.

Hasler, A., Gruber. S., Font. M., and Dubois. A.: Advective Heat Transport in Frozen Rock Clefts: Conceptual Model, Laboratory Experiments and Numerical Simulation, Permafrost and Periglacial Processes, 22, 378–389, https://doi.org/10.1002/ppp.737, 2011.

Hauck, C., Böttcher, M., and Maurer, H.: A new model for estimating subsurface ice content based on combined electrical and seismic data sets, The Cryosphere, 5, 453–468, https://doi.org/10.5194/tc-5-453-2011, 2011.

Hauck, C., and Hilbich C.: Preconditioning of mountain permafrost towards degradation detected by electrical resistivity. Environ. Res. Lett. 19 064010. https://doi.org/10.1088/1748-9326/ad3c55, 2024.

Herring, T., Lewkowicz, A. G., Hauck, C., Hilbich, C., Mollaret, C., Oldenborger, G. A., Uhlemann, S., Farzamian, M., Calmels, F., and Scandroglio, R.: Best practices for using electrical resistivity

875 tomography to investigate permafrost, Permafrost Periglac., 34, 494–512,
876 https://doi.org/10.1002/ppp.2207, 2023.
877 Hilbich, C., Marescot, L., Hauck, C., Loke, M. H., and Mäusbacher, R.: Applicability of Electrical
878 Resistivity Tomography Monitoring to Coarse Blocky and Ice-rich Permafrost Landforms,
879 Permafrost Periglac., 20, 269–284, https://doi.org/10.1002/ppp.652, 2009.
880 Hilbich, C., Hauck, C., Hoelzle, M., Scherler, M., Schudel, L., Völksch, I., Vonder Mühll, D., and
881 Mäusbacher, R.: Monitoring Mountain permafrost evolution using electrical resistivity
882 tomography: A 7-year study of seasonal, annual, and long-term variations at Schilthorn, Swiss
883 Alps, J. Geophys. Res.-Earth, 113, F01S90, https://doi.org/10.1029/2007JF000799, 2008.
884 Jacquemart, M., Weber, S., Chiarle, M., Chmiel, M., Cicoira, A., Corona, C., Eckert, N., Gaume, J.,
885 Giacona, F., Hirschberg, J., Kaitna, R., Magnin, F., Mayer, S., Moos, C., van Herwijnen, A., and
886 Stoffel, M.: Detecting the impact of climate change on alpine mass movements in observational
887 records from the European Alps, Earth-Science Reviews, 258, 104886,
888 https://doi.org/10.1016/j.earscirev.2024.104886, 2024.
889 Karaoulis, M., Tsourlos, P., Kim, J., and Revil, A.: 4D time-lapse ERT inversion: introducing combined
890 time and space constraints, Near Surf. Geophys., 12, 25–34, https://doi.org/10.3997/1873-
891 0604.2013004, 2013.
892 Keuschnig, M., Krautblatter,M., Hartmeyer, I., Fuss, C. and Schrott, L.: Automated electrical resistivity
893 tomography testing for early warning in unstable permafrost rock walls around Alpine
894 infrastructure, Permafrost Periglac., 28, 158–171. https://doi.org/10.1002/ppp.1916, 2017.
895 Krautblatter, M. and Hauck, C.: Electrical resistivity tomography monitoring of permafrost in solid rock
896 walls, J. Geophys. Res., 112, F02S20, https://doi.org/10.1029/2006JF000546, 2007.
897 Krautblatter M, Verleysdonk S, Flores-Orozco A., and Kemna A.: Temperature-calibrated imaging of
898 seasonal changes in permafrost rock walls by quantitative electrical resistivity tomography
899 (Zugspitze, German/Austrian Alps). J. Geophys. Res., 115, F02003,
900 https://doi.org/10.1029/2008JF001209, 2010.

Krautblatter, M., Funk, D. and G¨unzel, F.K.: Why permafrost rocks become unstable: a rock–ice-mechanical model in time and space. Earth Surf. Process. Landforms, 38, 876–887. https://doi.org/10.1002/esp.3374, 2013.

Loke, M. H.: Time-lapse resistivity imaging inversion, paper presented at 5th Meeting of the Environmental and Engineering Society European Section, Budapest. 1999.

Magnin, F., Deline, P., Ravanel, L., Noetzli, J., and Pogliotti, P.: Thermal characteristics of permafrost in the steep alpine rock walls of the Aiguille du Midi (Mont Blanc Massif, 3842 m a.s.l), The Cryosphere, 9, 109–121, https://doi.org/10.5194/tc-9-109-2015, 2015b.

Magnin, F., Krautblatter, M., Deline, P., Ravanel, L., Malet, E. and Bevington, A.: Determination of warm, sensitive permafrost areas in near-vertical rockwalls and evaluation of distributed models by electrical resistivity tomography, J. geophys. Res.-Earth, 120, 745–762, https://doi.org/10.1002/2014JF003351, 2015a.

Magnin, F., Ravanel, L., Bodin, X., Deline, P., Malet, E., Krysiecki, J.-M., et al.: Main results of permafrost monitoring in the French Alps through the PermaFrance network over the period 2010–2022. Permafrost and Periglacial Processes, 35(1), 3–23. https://doi.org/10.1002/ppp.2209, 2024.

Magnin, F. and Josnin, J.-Y.: Water flows in Rock Wall permafrost: a numerical approach coupling hydrological and thermal processes. Journal of Geophysical Research - Earth Surface, 126(11), e2021JF006394. https://doi.org/10.1029/2021JF006394, 2021.

Magnin, F., Josnin, J.-Y., Ravanel, L., Pergaud, J., Pohl, B., and Deline, P.: Modelling rock wall permafrost degradation in the Mont Blanc massif from the LIA to the end of the 21st century, The Cryosphere, 11, 1813–1834, https://doi.org/10.5194/tc-11-1813-2017, 2017.

Maierhofer, T., Flores Orozco, A., Roser, N., Limbrock, J. K., Hilbich, C., Moser, C., Kemna, A., Drigo, E., Morra di Cella, U., and Hauck, C.: Spectral induced polarization imaging to monitor seasonal and annual dynamics of frozen ground at a mountain permafrost site in the Italian Alps, The Cryosphere, 18, 3383–3414, https://doi.org/10.5194/tc-18-3383-2024, 2024.

Mewes, B., Hilbich, C., Delaloye, R., and Hauck, C.: Resolution capacity of geophysical monitoring regarding permafrost degradation induced by hydrological processes, The Cryosphere, 11, 2957–2974, https://doi.org/10.5194/tc-11-2957-2017, 2017.

929 Mollaret, C., Wagner, F. M., Hilbich, C., Scapozza, C., and Hauck, C.: Petrophysical Joint Inversion
930 Applied to Alpine Permafrost Field Sites to Image Subsurface Ice, Water, Air, and Rock Contents,
931 Front. Earth Sci., 8, 1–25, https://doi.org/10.3389/feart.2020.00085, 2020.
932 Mollaret, C., Hilbich, C., Pellet, C., Flores-Orozco, A., Delaloye, R., and Hauck, C.: Mountain
933 permafrost degradation documented through a network of permanent electrical resistivity
934 tomography sites, The Cryosphere, 13, 2557–2578, https://doi.org/10.5194/tc-13-2557-2019, 2019.
935 Noetzli J., Gruber S., Kohl T., Salzmann N., Haeberli W.: Three-dimensional distribution and evolution
936 of permafrost temperatures in idealized high-mountain topography. Journal of Geophysical
937 Research: Earth Surface 112, n/a–n/a. https://doi.org/10.1029/2006JF000545, 2007.
938 Noetzli, J., Isaksen, K., Barnett, J. et al.: Enhanced warming of European mountain permafrost in the
939 early 21st century. Nat Commun 15, 10508. https://doi.org/10.1038/s41467-024-54831-9, 2024.
940 Moser, C., Morra di Cella, U., Hauck, C., and Flores Orozco, A.: Spectral induced polarization survey
941 for the estimation of hydrogeological parameters in an active rock glacier, The Cryosphere, 19,
942 143–171, https://doi.org/10.5194/tc-19-143-2025, 2025.
943 Offer, M., Weber, S., Krautblatter, M., Hartmeyer, I., and Keuschnig, M.: Pressurised water flow in
944 fractured permafrost rocks revealed by borehole temperature, electrical resistivity tomography, and
945 piezometric pressure, The Cryosphere, 19, 485–506, https://doi.org/10.5194/tc-19-485-2025, 2025.
946 Pavoni, M., Boaga, J., Wagner, F. M., Bast, A., Phillips, M.: Characterization of rock glaciers
947 environments combining structurally-coupled and petrophysically-coupled joint inversions of
948 electrical resistivity and seismic refraction datasets, Journal of Applied Geophysics, 215, 0926-
949 9851, https://doi.org/10.1016/j.jappgeo.2023.105097, 2023.
950 Piolat, L., Revil, A., Richard, J., Ghorbani G., Cosme, P., Géraud, Y., Casotti, C., Vaudelet, P., Diraison,
951 M., and Favier, A.: Induced polarization of volcanic rocks. 8. The case of intrusive igneous
952 rocks, *Geophysical Journal International*, Volume 241, Issue 2, Pages 1348
953 1372, https://doi.org/10.1093/gji/ggaf102, 2025.
954 Ravanel, L., Magnin, F. and Deline, P.: Impacts of the 2003 and 2015 summer heatwaves on permafrost-
955 affected rock-walls in the Mont Blanc massif. Science of the Total Environment, 609, 132–143.
956 https://doi.org/10.1016/j.scitotenv.2017.07.055, 2017.

957 Revil, A., Cathles, L. M., Losh, S., & Nunn, J. A.: Electrical conductivity in shaly sands with
958 geophysical applications. Journal of Geophysical Research, 103(B10), 23,925–23,936.
959 https://doi.org/10.1029/98JB02125, 1998.
960 Revil, A., Ghorbani, A., Zhao, X., Mouyeaux, A., Barrère, L., Richard, J., Peyras, L., and Vaudelet, P.:
961 Groundwater flow paths using combined self-potential, electrical resistivity, and induced
962 polarization signals, Geophysical Journal International, 239, 2, 798–
963 820, https://doi.org/10.1093/gji/ggae291, 2024.
964 Revil, A., Coperey, A., Mao, D., Abdulsamad, F., Ghorbani, A., Rossi, M., and Gasquet, D,.: Induced
965 polarization response of porous media with metallic particles — Part 8: Influence of temperature
966 and salinity: Geophysics, 83, no. 6, E435–E456, https://doi.org/10.1190/geo2018-0089.1, 2018.
967 Revil A., J. Richard, A. Ghorbani, F. Magnin, P.A. Duvillard, M. Marcer, F. Abdulsamad, T. Ingeman-
968 Nielsen, L. Ravanel, C. Lambiel, X. Bodin, H. Cai, X. Hu, and P Vaudelet.: Induced polarization
969 as a tool to characterize permafrost 1. Theory and laboratory experiments, Geophysical Journal
970 International, 244, 1. https://doi.org/10.1093/gji/ggaf443, 2026a.
971 Revil A., P. A. Duvillard, M. Marcer, J. Richard, T. Ingeman-Nielsen, F. Abdulsamad, F. Magnin, B.
972 Charonnat, H. Cai, X. Hu, L. Ravanel, and P. Schoeneich.: Induced polarization as a tool to
973 characterize permafrost. 2. Applications to low and high-porosity environments, Geophysical
974 journal International, 244, 1. https://doi.org/10.1093/gji/ggaf464, 2026b.
975 Rücker, C., Günther, T., and Wagner, F. M.: pyGIMLi: An open-source library for modelling and
976 inversion in geophysics, Computers & Geosciences, 109, 106–123,
977 https://doi.org/10.1016/j.cageo.2017.07.011, 2017.
978 Sass, O.: Rock Moisture Fluctuations During Freeze-thaw Cycles: Preliminary Results from Electrical
979 Resistivity Measurements, Polar Geogr., 28, 13–31, https://doi.org/10.1080/789610157, 2004.
980 Scandroglio, R., Draebing, D., Offer, M., Krautblatter, M.: 4D quantification of alpine permafrost
981 degradation in steep rock walls using a laboratory-calibrated electrical resistivity tomography
982 approach, Near Surface Geophys., 19, 241-260, https://doi.org/10.1002/nsg.12149, 2021.
983 Smith, S.L., O'Neill, H.B., Isaksen, K. et al.: The changing thermal state of permafrost. Nat Rev Earth
984 Environ 3, 10–23. https://doi.org/10.1038/s43017-021-00240-1, 2022.

985 Steiner, M., Wagner, F. M., and Flores Orozco, A.: Improved characterization of alpine permafrost
986 through structurally constrained inversion of refraction seismic data, The Cryosphere Discuss,
987 https://doi.org/10.5194/tc-2019-52, 2019.
988 Steiner, M., Wagner, F. M., Maierhofer, T., Schöner, W., and Flores Orozco, A.: Improved estimation
989 of ice and water contents in alpine permafrost through constrained petrophysical joint inversion:
990 The Hoher Sonnblick case study, Geophysics 86: WB61-WB75. https://doi.org/10.1190/geo2020-
991 0592.1, 2021.
992 Wagner, F. M., Mollaret, C., Kemna, A., and Hauck, C.: Quantitative imaging of water, ice and air in
993 permafrost systems through petrophysical joint inversion of seismic refraction and electrical
994 resistivity data, Geophys. J. Int., 219, 1866–1875, https://doi.org/10.1093/gji/ggz402, 2019.
995 Zimmermann, E., Kemna, A., Berwix, J., Glaas, W., Münch, H. M., and Huisman, J. A.: A high accuracy
996 impedance spectrometer for measuring sediments with low polarizability. Measurement Science
997 and Technology, 19(10), 105603. https://doi.org/10.1088/0957-0233/19/10/105603, 2008.